NOTE TO USERS

Nonlinear Viscoelasticity and Wall Slip of Molten Polymers

by

Junke Xu

Department of Chemical Engineering

McGill University, Montreal

January 2005

A thesis submitted to the Faculty of Graduate Studies in partial fulfillment of the requirement of the degree of Master of Engineering

Your file Votre référence
ISBN: 0-494-12658-2
Our file Notre référence
ISBN: 0-494-12658-2

Abstract

Two nearly monodisperse polybutadienes (PBd) having different molecular weights were used to study nonlinear viscoelastic behavior using a sliding plate rheometer incorporating shear and normal stress transducers.

Comparison of data for the shear stress growth function at the start-up of steady simple shear with predictions of the Wagner model was used to estimate the time-dependency of wall slip. Both the time-dependent slip velocity and the steady-state values were found to depend on molecular weight, thus supporting the hypothesis that "slip" actually involves a shear-induced disentanglement between molecules strongly adsorbed at the wall and those in the bulk. The critical shear stress for the onset of slip was about 230kPa for both PBds, suggesting that the critical stress is independent of molecular weight and related to the plateau modulus. Slip behavior on steel and glass substrates was quite similar. Rubber-like high-molecular-weight polybutadiene exhibited well-defined, steady, normal stresses at moderate shear rates, while molten polystyrene exhibited a steady normal stress up to much higher shear rates.

Step strain data were used to determine the time and strain dependency of the nonlinear relaxation modulus. Time-strain factorability was observed, and the damping function was determined. For the moderately entangled PBd2 the experimentally determined damping function agreed with the predictions of the Doi-Edwards constitutive model and thus the Lodge-Meissner relationship. The higher molecular weight PBd3 exhibited strong wall slip.

Résumé

Deux polybutadiènes (PBd) ayant différents poids moléculaires ont été employés pour l'étude de leur comportement viscoélastique non linéaire à l'aide d'un rhéomètre à glissement de plateaux incorporant des capteurs de cisaillement et de stress normal.

La comparaison entre la fonction d'accroissement du stress de cisaillement suite à l'application d'un cisaillement simple et régulier avec les prédictions du modèle de Wagner a été utilisée pour estimer la dépendance temporelle du glissement du mur. Les valeurs de vélocité du mur en fonction du temps et de la contrainte semblent dépendre du poids moléculaire, supportant l'hypothèse que le mur implique un cisaillement et induit un désenchevêtrement entre les molécules fortement adsorbées au mur et les autres. Le stress de cisaillement critique initial appliqué sur le mur était d'environ 230 kPa pour les deux PBds, suggérant que le stress critique est indépendant du poids moléculaire et relié au module de plateau. Le comportement du mur sur des substrats d'acier et de verre est relativement similaire. Les polybutadiènes de haut poids moléculaire, apparentés au caoutchouc démontrent un stress normal bien défini et régulier à un taux de cisaillement modéré alors que le polystyrène fondu démontre un stress normal régulier à un taux de cisaillement beaucoup plus élevé.

Des données de contrainte d'étape ont été utilisées pour déterminer la dépendance du module de relaxation non linéaire au temps et à la contrainte. Un facteur temps-contrainte a été observé, et la fonction d'atténuation a été déterminée. Pour le PBd2 modérément enchevêtré la fonction d'atténuation expérimentale est en accord avec les prédictions du modèle constitutif de Doi-Edwards et donc avec le rapport de Lodge-Meissner. Le PBd3 de plus haut poids moléculaire démontre un fort glissement du mur.

Acknowledgements

The guidance, support and patience of Professor John Dealy in seeing this document to completion are gratefully acknowledged. His rigorous, profound approach to polymer rheology had a tremendous impact on the overall quality of this research.

I express my special appreciation to Dr. Hee Eon Park for his kind supports on SPR experiments, valuable helps and fruitful discussions, and to Dr. Chunxia He for her useful suggestions and being a great mentor to me in the study of linear viscoelasticity.

Many thanks to Charles Dolan and Alain Gagnon of the Chem-Met machine shop who were very helpful in continuously optimizing the rheometers for use in this project. In particular I want to thank Charles Dolan for his prompt attention to many calls for help. Also I wish to acknowledge Frank Caporuscio for his technical support.

I would like to thank Dr. Christopher Robertson and Dr. Mark DeDecker in the Firestone Polymer Company for making the indispensable, nearly monodisperse polybutadiene that were used in this work.

I extend my thanks to Matthew Campbell, Fabricio Smillo, Jen Shueng Tiang, Dr. Sung Taek Lim for their generous cooperation and friendship in polymer rheology laboratory.

List of Figures

List of Tables

Table of Contents

Chapter 1 Introduction

1.1 Motivation for Work

Linear viscoelasticity is very useful for polymer characterization. However, the linear properties only describe flow behaviour when the deformation is either very small or very slow, whereas polymer processing always involves large, rapid deformations. In such operations, polymer molecules are oriented and stretched, for example in melt spinning, film blowing and wire coating. Thus, nonlinear viscoelastic phenomena play a prominent role in polymer processing. In order to investigate the nonlinear behavior of polymer melts it is necessary to use a technique that can generate both orientation and stretch. Examples of nonlinear phenomena exhibited during shear are stress overshoot during start-up flow and the normal stresses that result from shear-induced anisotropy.

High molecular weight melts respond to large, rapid deformations in a way that is similar in some ways to that of a cross-linked rubber. This led to the modeling of the interaction between macromolecules in terms of temporary cross-links. However, more recent models see a macromolecule as moving through a contorted tube consisting of topological constraints imposed by surrounding molecules. This motion was called "reptation" by de Gennes [1], and this approach was applied to molten polymers by Doi and Edwards [2]. There is a general consensus that the relaxation molulus $G(t)$ of linear polymer melts is described successfully by the Doi-Edwards theory. The basic theory, together with various refinements, yields predictions that compare favourably with observations of the linear viscoelastic properties of monodisperse, highly-entangled polymers. Modelling the response to large, rapid deformations, however, requires the introduction of additional relaxation mechanisms, in particular, retarded retraction after strain-induced chain stretch and convective constraint release in high-rate flows.

Rheological measurements are used reveal the transient nature of molecular interactions in a variety of deformations. The most-used shear tests are start-up of steady simple shear and stress relaxation following a step strain. Conventional, rotational rheometers, however, are limited in their ability to subject a sample to a uniform shearing

at a high strain rate. The lack of accurate data describing the nonlinear viscoelastic behavior of melts provided the motivation for the present study. The sliding plate rheometer (SPR) was developed at McGill University to make reliable measurements of the shear stress and first normal stress difference during large, rapid transient shearing deformations. Such data are essential for the evaluation of theoretical predictions and to predict the processing behaviour of entangled polymer melts.

1.2 The Viscoelasticity of Polymer Melts

When an ideal, elastic solid is subjected to a deforming force, it will instantly reach its equilibrium deformation. This is in accordance with Hook's law, wherein stress is proportional to strain and independent of strain rate. The deformation of an ideal viscous liquid, conversely, will deform at a constant rate under a constant force, and Newton's law of viscosity states that stress is proportional to strain rate and independent of the strain itself. However, the behaviour of a polymeric material is time-dependent, occupying an intermediate position between those of the ideal elastic solid and the ideal viscous liquid. Thus, a polymer is a viscoelastic material, and its viscoelastic behavior is one of the most significant and complex physical properties of a polymer.

In a very dilute polymer solution, viscoelasticity is a relatively minor perturbation of the Newtonian behaviour of the solvent, because the polymer molecules are sufficiently separated to move independently. And for very low molecular weight polymeric liquids, the effect of neighbouring molecules on viscoelastic properties can be described in terms of local frictional forces encountered by short segments of the chain. However, the molecular chain in polymer melts above a critical molecular weight reveal a strong entanglement coupling to neighbors which acts as though it were localized at a few widely separated points along the chain. The topological constraints represented by entanglement dramatically limit the motion of a target molecule. The detailed nature of these constraints is not well understood. However, the most significant consequence of these interactions is the pronounced viscoelasticity.

Viscoelastic behavior is divided into two regimes: linear viscoelasticity, and non-linear viscoelasticity. The theory of linear viscoelasticity began with the study of stress

relaxation by Maxwell, continued with the study of elastic residual effects by Kelvin and Voigt. The general principle governing linear viscoelasticity is the Boltzmann superposition principle (BSP). There is substantial literature on the modeling of these two regimes, but the following review will focus on the physical concepts underlying viscoelastic behavior and continuum models developed to predict the behaviour of entangled polymer melts.

1.3 Linear Viscoelasticity

The simplest type of viscoelastic behavior is linear viscoelasticity (LVE). This type of behavior is observed when the deformation is sufficiently mild that polymer molecules are disturbed from their equilibrium configuration to a negligible extent. A very small deformation or a large one that occurs very slowly would fall into this category. In a very small deformation, a molecule departs from its equilibrium state to a negligible degree and in a very slow deformation relaxation processes due to Brownian motion are able to maintain a molecule in its equilibrium state. Viscoelastic properties such as viscosity and relaxation modulus in this category are independent of deformation rate or magnitude.

1.3.1 Phenomenology

There are four experimental methods commonly used to study linear viscoelastic behavior:

1. Measure the stress as a function of time when a material is subjected to a sudden strain γ starting at time $t=0$. The relaxation modulus is defined as:

$$G(t)\equiv\sigma(t)/\gamma \tag{1-1}$$

2. Measure the stress as a function of time when a material is subjected to a constant strain rate starting at time $t=0$. This experiment is called start-up of steady simple shear. The shear stress and the first normal stress growth coefficients are defined as follows:

$$\eta^{+}(t)\equiv\sigma(t)/\dot{\gamma} \tag{1-2}$$

$$\Psi_1^+(t) \equiv N_1(t) / \dot{\gamma}^2 \quad (1\text{-}3)$$

3. Measure the strain as a function of time when a material is subjected to a sudden constant stress σ at time $t=0$. This is referred to as a creep experiment. The resulting material function is called the shear creep compliance and is defined as:

   $$J(t) \equiv \gamma(t)/\sigma \quad (1\text{-}4)$$

   After a sufficiently long time, the strain rate becomes constant, and the compliance can be represented as $J(t) = J_s^0 + t/\eta_0$, where J_s^0 is the steady state compliance and η_0 is the zero-shear viscosity.

4. Measure the stress during small-amplitude oscillatory shear. From the BSP, it can be shown that the stress will also be sinusoidal:

   $$\gamma(t) = \gamma_0 \sin \omega t \quad (1\text{-}5)$$

   $$\sigma(t) = \sigma_0 \sin(\omega t + \delta) = \sigma_0(\sin \omega t \cos\delta + \cos \omega t \sin\delta) \quad (1\text{-}6)$$

   The results are usually reported in terms of the storage G' and loss moduli G'':

   $$G' = \sigma_0 \cos\delta / \gamma_0 \quad (1\text{-}7)$$

   $$G'' = \sigma_0 \sin\delta / \gamma_0, \text{ where } \delta \text{ is a phase shift.} \quad (1\text{-}8)$$

The assumption in the theory of linear viscoelasticity is that the deformation imposed on the material is sufficiently small or slow that the macromolecular orientation and shape are unchanged from the undeformed state. Dilute polymeric solutions are characterized by the total lack of interaction between macromolecules. Therefore the viscoelastic properties of these materials—such as viscosity and relaxation modulus—are solely a consequence of time-dependent changes in conformation and orientation when the polymer is deformed by the solvent; there is no interaction between the molecules. However, in concentrated solutions and molten polymers a major complication arises, which is called "entanglement coupling." The modern view of macromolecular interactions is that the phenomena attributed to entanglements are actually topological effects associated with the inability of chains to pass through each other.

1.3.2 Boltzmann Superposition Principle & Relaxation Spectrum

Taking stress relaxation as an example, Boltzmann proposed that: (1) a material's relaxation behaviour depends on its entire deformation history; (2) every incremental strain independently contributes to the stress relaxation. Therefore, the stress at time t can be calculated by summing the contributions made by each strain that occurred at previous times, t'.

In the computation of one linear viscoelastic function from another, it is sometimes convenient to replace this discrete model by a continuous relaxation spectrum. This can be defined by letting the number of elements in the generalized Maxwell model increase to infinity so that $G(t)$ can be represented in terms of the continuous function, $F(\lambda)$. Thus, $Fd\lambda$ is the contribution to the relaxation modulus from relaxation times between λ and $\lambda+d\lambda$. In general, $H(\lambda)$ is often used in place of $F(\lambda)$, because it is convenient to use a logarithmic time scale, where $H=F\lambda$, and $Hd(ln\lambda)=Fd\lambda$.

In terms of $G(t)$ and $H(\lambda)$, the material functions of the four basic experiments (Eqs. 1-1 to 1-8) can be written as shown in Eqs. 1-9 to 1-12:

1. Stress relaxation:

$$\sigma(t) = \int_{-\infty}^{t} G(t-t')d\gamma(t'); \tag{1-9}$$

$$G(t) = \int_{-\infty}^{+\infty} H(\lambda)[\exp(-t/\lambda)]d(\ln\lambda) \tag{1-10}$$

2. Start-up of steady simple shear:

$$\eta^+(t) = \int_0^t G(s)ds = \int_{-\infty}^{t} H(\lambda)\lambda d(\ln\lambda) \tag{1-11}$$

$$\Psi_1^+(t) = 2\int_0^t G(s)sds = 2\int_{-\infty}^{t} H(\lambda)\lambda^2 d(\ln\lambda) \tag{1-12}$$

The low-shear-rate limiting viscosity, η_0, and the first normal stress coefficient, $\Psi_{1,0}$, are given by:

$$\eta_0 = \lim_{\dot{\gamma}\to 0}\eta(\dot{\gamma}) = \int_0^{\infty} G(s)ds = \int_{-\infty}^{+\infty} H(\lambda)\lambda d(\ln\lambda) \tag{1-13}$$

$$\Psi_{1,0} = \lim_{\dot{\gamma} \to 0} \frac{N_1(\dot{\gamma})}{\dot{\gamma}^2} = 2\int_0^\infty G(s)sds = 2\int_{-\infty}^{+\infty} H(\lambda)\lambda^2 d(\ln\lambda) \tag{1-14}$$

3. Creep:

$$J_S^0 = \frac{\int_0^\infty G(s)sds}{\left[\int_0^\infty G(s)ds\right]^2} = \frac{\int_{-\infty}^{+\infty} H(\lambda)\lambda^2 d(\ln\lambda)}{\left[\int_{-\infty}^{+\infty} H(\lambda)\lambda d(\ln\lambda)\right]^2} \tag{1-15}$$

4. Small amplitude oscillatory shear:

$$G'(\omega) = \omega\int_0^\infty G(s)\sin(\omega s)ds = \int_{-\infty}^{+\infty}[H(\lambda)\omega^2\lambda^2/(1+\omega^2\lambda^2)]d(\ln\lambda)$$

$$G''(\omega) = \omega\int_0^\infty G(s)\cos(\omega s)ds = \int_{-\infty}^{+\infty}[H(\lambda)\omega\lambda/(1+\omega^2\lambda^2)]d(\ln\lambda) \tag{1-16}$$

1.4 Non-Linear Viscoelasticity

As stated in section 1.3.1, linear viscoelascity theory is valid only when the deformation is very small or very slow. But the processes used to form polymers into commercial products always involve large, rapid deformations, in which polymer molecules are strongly oriented and stretched as a result. For these large and rapid deformations, the linear theory is no longer valid. In the category of nonlinear viscoelastic behavior, the material functions discussed above will be dependent on both time and strain, or strain rate. For example, $G(t)$ and $\eta^+(t)$, become $G(t, \gamma)$ and $\eta^+(t, \dot{\gamma})$. The nonlinear relaxation modulus is often found to be separable into time-dependent and strain-dependent factors, so that $G(t,\gamma)=G(t)h(\gamma)$, where $h(\gamma)$ is called the damping function.

For the above reason, in order to study nonlinear behavior we must employ a rheological technique capable of generating molecular orientation and stretch. It has long been thought that significant stretch could be generated only in extensional flows. However, recent theoretical models indicate that transient shear flows can generate significant stretch. Likely flow candidates are: 1) exponential shear; 2) large-step shear,

which is the only direct way to verify the separability of the nonlinear relaxation modulus and determine the damping function; 3) start-up of steady simple shear, which is the flow that is the easiest to generate in the laboratory because it is the velocity, rather than the position of the moving surface that is controlled. Shear flow is also of industrial importance because the forming processes of many plastics involve shear. While step-shear at large strain definitely generates stretch, melts are known to exhibit slip in this experiment, and this greatly limits the amount of strain that can be generated. Of the shear flows listed above, model calculations indicate that start-up of steady simple shear is best for generating significant stretch.

1.4.1 Large-Step Shear Strain

Before outlining what information can be extracted from a step shear test, it is necessary to describe the test in terms of a nonlinear strain measure. The BSP, described in 1.2.2, is only valid for very small or very slow deformations. It uses an infinitesimal strain measure that is not frame-invariant, and the frame-invariant Finger tensor denoted as $B_{ij}(t, t')$ [3], is widely used as a finite measure of strain. This measure of strain is used in a theory of finite linear viscoelasticity proposed by Lodge [4] and called the "rubber-like liquid" model, which is given by Eq. 1-17.

$$\tau_{ij}(t) = \int_{-\infty}^{t} m(t-t')B_{ij}(t,t')dt', \qquad \text{where } m(t-t') \text{ is memory function} \qquad (1\text{-}17)$$

For the purposes of this thesis, it will be sufficient to know the components of this tensor for the simple shear, and these are given by Eq. 1-18.

$$B_{ij}(t,t') = \begin{pmatrix} 1+\gamma_{t,t'}^2 & \gamma_{t,t'} & 0 \\ \gamma_{t,t'} & 1 & 0 \\ 0 & 0 & 1 \end{pmatrix}, \qquad \text{where } \gamma_{t,t'} \equiv \gamma(t') - \gamma(t). \qquad (1\text{-}18)$$

Thus, for any simple shear deformation, from Eqs. 1-17 and 1-18, we have:

$$\sigma(t) \equiv \tau_{21}(t) = \int_{-\infty}^{t} m(t-t')\gamma_{t,t'}dt' \qquad (1\text{-}19)$$

Integrating by parts and noting that $G(\infty)=0$, Eq. 1-19 becomes:

$$\sigma(t) = \int_{-\infty}^{t} G(t-t')d\gamma(t') \tag{1-20}$$

This is the same as Eq. 1-9, so the predictions of the rubber-like liquid model for the shear stress in any simple shear flow are the same as those of the Boltzmann superposition principle. However, unlike the BSP, the rubber-like liquid model does predict a nonzero first normal stress difference N_1:

$$N_1(t) \equiv \sigma_{11} - \sigma_{22} = \int_{-\infty}^{t} m(t-t')\gamma_{t,t'}^2 dt' \tag{1-21}$$

A more general "continuum" (empirical) model of nonlinear viscoelasticity, which is capable of qualitatively describing additional features of nonlinear behaviour, is the BKZ model:

$$\tau_{ij}(t) = \int_{-\infty}^{t} M[(t-t'), I_1(B_{ij}), I_2(B_{ij})]B_{ij}(t,t')dt' \tag{1-22}$$

where I_1 and I_2 are scalar invariants of the Finger tensor: $I_1(B_{ij}) = \mathrm{tr}(B_{ij}) = B_{11}+B_{22}+B_{33}$; $I_2(B_{ij}) = \mathrm{tr}(B_{ij}^{-1}) = B_{11}^{-1}+B_{22}^{-1}+B_{33}^{-1}$.

Wagner [5] proposed to write the memory function $M[(t-t'), I_1(B_{ij}), I_2(B_{ij})]$ as a product of a strain-independent function of time $[m(t,t')]$ and a function of strain only, $h(I_1, I_2)$, which is called the damping function:

$$\tau_{ij}(t) = \int_{-\infty}^{t} m(t-t')h(I_1, I_2)B_{ij}(t,t')dt' \tag{1-23}$$

As we are interested only in shear behaviour, the invariants of the Finger tensor are given by: $I_1 = I_2 = (\gamma^2_{t,t'} + 3)$ are replaced by $\gamma_{t,t'}$. Thus, for simple shear flow the generalized memory function can be expressed as:

$$m(t-t'; \gamma_{t,t'}) = m(t-t')h(\gamma_{t,t'}) \tag{1-24}$$

Eq. 1-24 represents a special case of the BKZ model in which the nonlinearity enters into the memory function only in terms of the damping function $h(\gamma_{t,t'})$, which is a function only of the shear strain. For $h(\gamma_{t,t'})=1$, the Lodge rubberlike liquid is recovered. However, nonlinear behavior always implies that $h(\gamma_{t,t'}) < 1$.

Consider a step shear strain experiment described by:

$$\gamma_{t,t'} = \begin{cases} 0 & \text{for } t\text{-}t' < t \\ \gamma & \text{for } t\text{-}t' \geq t \end{cases} \tag{1-25}$$

Using Eqs. 1-19, 1-24, and 1-25 one can obtain the shear relaxation modulus $G(t,\gamma)$ which describes the relaxation of the shear stress σ.

$$G(t,\gamma) = \frac{\sigma(t)}{\gamma} = \frac{1}{\gamma}\int_{t}^{\infty} m(t-t')h(\gamma)\gamma d(t-t') = G(t)h(\gamma). \tag{1-26}$$

where $G(t) \equiv \frac{\sigma(t)}{\gamma} = \int_{-\infty}^{0} m(t-t')dt'$ (1-27)

Step shear is the most straightforward method to verify the time-strain separability of the nonlinear relaxation modulus and to determine the damping function $h(\gamma)$ when $G(t,\gamma)$ is separable. As an approximation of the damping function, Wagner [5] proposed a single exponential function:

$$h(\gamma)=exp\,[-n\gamma] \tag{1-28}$$

The parameter n is determined from experimental data for start-up of steady simple shear, which is discussed in the next section.

The general form of $h(I_1, I_2)$ for deformations other than simple shear remains unknown. Moreover, $h(I_1,I_2)$ is material specific. Therefore, there is no practical way to determine this function experimentally. Since $h(I_1, I_2)$ is not known, Wagner's equation (Eq. 1-23) is not a complete constitutive equation. However, presently available evidence suggests that this equation can describe the general characteristics of the response to simple shear strain histories. For example, one can use $h(\gamma)$ to predict the viscosity function $\eta(\dot{\gamma})$ and $\eta^{+}(t, \dot{\gamma})$ for start-up of steady simple shear. Likewise, relaxation of the first normal stress difference is described by the modulus $G_{N_1}(t,\gamma)$. Using Eqs. 1-21, 1-24, and 1-25 one obtains

$$G_{N_1}(t,\gamma) = \frac{N_1(t)}{\gamma^2} = \frac{1}{\gamma^2}\int_{t}^{\infty} m(t-t')h(\gamma)\gamma^2 d(t-t') = G(t)h(\gamma). \tag{1-29}$$

By comparing Eqs.1-26 and 1-29, it is seen that the moduli determined from the relaxation of the shear stress and from the relaxation of the first normal stress difference are identical. Therefore, we find:

$$\frac{N_1(t)}{\sigma(t)} = \gamma \tag{1-30}$$

Eq. 1-30 is called the Lodge-Meissner relations [6,7] and has often been observed to hold for molten polymers beyond the normal range of validity of the rubber-like liquid model. In fact, this relation has been found to be valid up to substantial strain values.

1.4.2 Start-up of Steady Simple Shear

Steady simple shear (SSS) is carried out at a constant shear rate; after a sufficient length of time that the stresses are constant, the three measurable material functions are $\sigma(\dot{\gamma})$, $N_1(\dot{\gamma})$, and $N_2(\dot{\gamma})$, which are usually reported in terms of the viscometric functions:

Viscosity: $\eta \equiv \sigma / \dot{\gamma}$;

First normal stress coefficient: $\Psi_1 \equiv N_1 / \dot{\gamma}^2$;

Second normal stress coefficient: $\Psi_2 \equiv N_2 / \dot{\gamma}^2$. (1-31)

Additional information is provided by measuring the stresses as functions of time at start-up of steady simple shear. Corresponding to the steady shear (viscometric) properties are the following transient material functions:

Start-up shear stress: $\sigma^+ \equiv \sigma(t, \dot{\gamma})$ (1-32)

Shear stress growth coefficient: $\eta^+(t, \dot{\gamma}) \equiv \sigma^+ / \dot{\gamma}$ (1-33)

First normal stress growth function: $N_1^+(t, \dot{\gamma}) \equiv \sigma_{11}(t, \dot{\gamma}) - \sigma_{22}(t, \dot{\gamma})$ (1-34)

Second normal stress growth function: $N_2^+(t, \dot{\gamma}) \equiv \sigma_{22}(t, \dot{\gamma}) - \sigma_{33}(t, \dot{\gamma})$ (1-35)

First normal stress growth coefficient: $\Psi_1^+(t, \dot{\gamma}) \equiv N_1^+(t, \dot{\gamma}) / \dot{\gamma}^2$ (1-36)

Second normal stress growth coefficient: $\Psi_2^+(t, \dot{\gamma}) \equiv N_2^+(t, \dot{\gamma}) / \dot{\gamma}^2$ (1-37)

After the sudden imposition of a constant shear rate, the shear history of stress growth $\dot{\gamma}$ is defined by

$$\gamma_{t,t'} = \begin{cases} \dot{\gamma}(t\text{-}t') & \text{for } t\text{-}t' < t \\ \dot{\gamma}\, t & \text{for } t\text{-}t' \geq t \end{cases} \tag{1-38}$$

Using Wagner's single-exponential damping function, Eq.1-28, the time dependence of the shear stress (Eq. 1-19) and the first normal stress difference (Eq. 1-21) are as follows:

$$\sigma(t) = \int_{-\infty}^{t} m(t-t')\exp(-n\gamma_{t,t'})\gamma_{t,t'}dt' \tag{1-39}$$

$$N_1(t) = \int_{-\infty}^{t} m(t-t')\exp(-n\gamma_{t,t'})\gamma_{t,t'}^2 dt' \tag{1-40}$$

Taking Eq. 1-38 into Eqs. 1-39 and 1-40, letting $s=t\text{-}t'$, and employing Eqs. 1-33 and 1-36, we can calculate the corresponding stress growth functions:

$$\eta^+(t,\dot{\gamma}) = \int_0^t G(s)[\exp(-n\dot{\gamma}s)](1-n\dot{\gamma}s)ds \tag{1-41}$$

$$\Psi_1^+(t,\dot{\gamma}) = \int_0^t G(s)s[\exp(-n\dot{\gamma}s)](2-n\dot{\gamma}s)ds \tag{1-42}$$

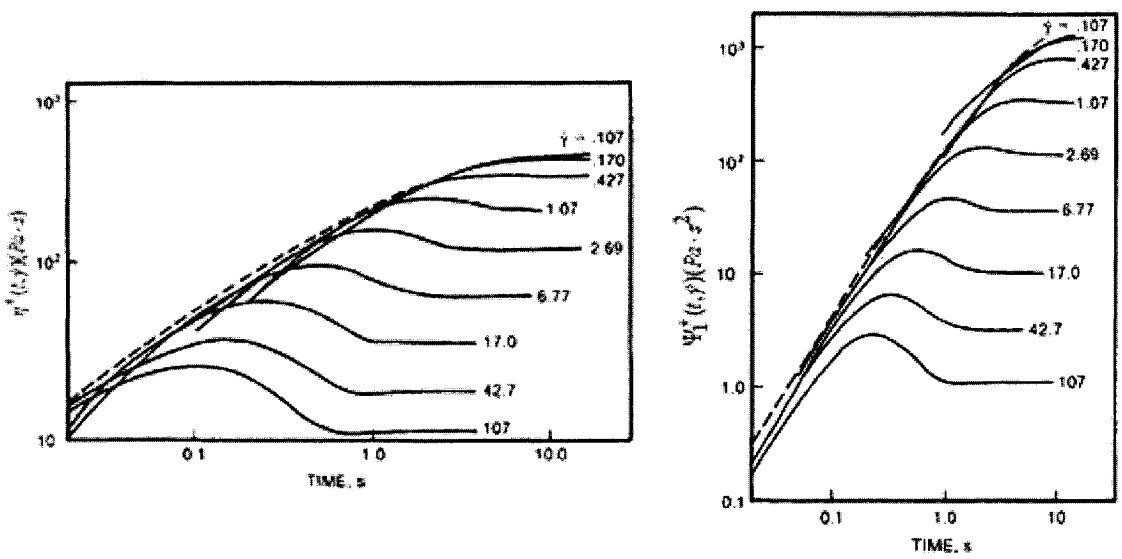

Figure 1-1 Shear stress (left) and the first normal stress (right) growth function for a polystyrene solution [8].

Figure 1-1 shows the typical curves for $\eta^+(t,\dot{\gamma})$ and $\Psi_1^+(t,\dot{\gamma})$ for a polystyrene solution [8]. The dashed curves are calculated from the linear spectrum using Eqs. 1-11 and 1-12. As the shear rate is increased, both curves deviate from the one for linear behavior at progressively shorter times. They also exhibit a stress overshoot with the maximum stress occurring at time t_S, and t_N, over the lowest decade of shear rates (Figure 1-2). These quantities are inversely proportional to the shear rate, implying that the maxima always occur at constant values of the shear strains γ_S and γ_N. Using Wagner's single exponential damping function Eq.1-28, the following relations are obtained:

$$\gamma_S = \dot{\gamma} \cdot t_S = \frac{1}{n} \tag{1-43}$$

$$\gamma_N = \dot{\gamma} \cdot t_N = \frac{2}{n} \tag{1-44}$$

$$\frac{\gamma_N}{\gamma_S} = \frac{t_N}{t_S} = 2 \tag{1-45}$$

These relations provide the basis for estimating the damping function parameter n by plotting t_S and t_N as functions of $\dot{\gamma}$.

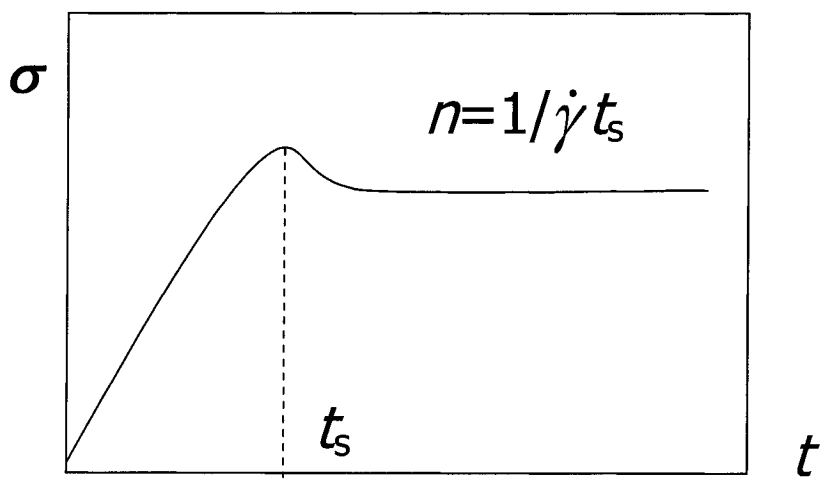

Figure 1-2 Determination of t_s to reach maximum shear stress.

1.5 Wall Slip

"Wall slip" is an adhesive or cohesive failure occurring in a polymer melt at, or very near, a solid interface at a critical shear stress, σ_c. It is generally agreed that melts do not detach from high-energy surfaces at high stress but instead undergo disentanglement from a layer of strongly adsorbed molecules near the wall. In rectilinear flow, slip occurs along a failure plane parallel to the bounding surface [9]. There is strong evidence that wall slip plays a role in some of the extrudate distortions observed in melt processing [10] and is an unavoidable aspect of the behavior of highly entangled, linear melts and elastomers.

When slip occurs the velocity is not zero at the interface and the shear rate calculated in the normal way is only a nominal shear rate rather than the true shear rate within the melt. Therefore, the true shear rate and corresponding stress response are reduced. Figure 1-3 depicts slip at the walls as it occurs in a sliding plate, where V is the moving plate velocity and V_s the slip velocity. In addition, if the two walls are dissimilar (*i.e.* constructed of different materials) the critical stresses and the slip velocities may differ at the two walls.

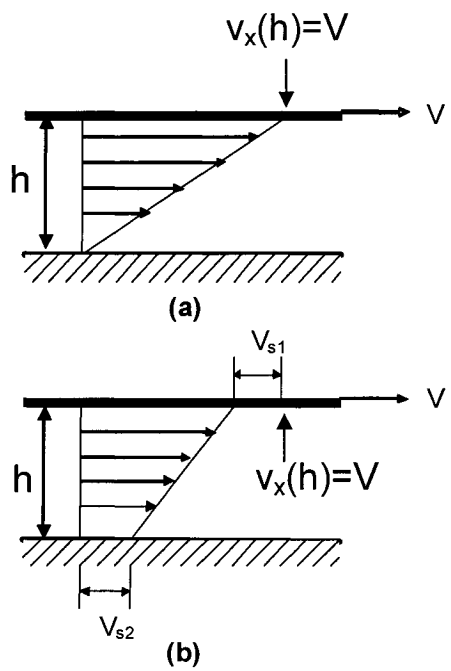

Figure 1-3 Cross-sectional view of the velocity profile in the parallel sliding plate geometry for (a) no slip flow, and (b) flow with slip.

Many experimental studies of slip in rheometers [11,12,13,14] have been reported. These indicate that wall slip does not result from adhesive failure at a steel surface, but is instead a reversible coil-stretch transition of adsorbed polymer molecules that leads to a disentanglement of molecules between those strongly adsorbed at the wall and those in the flowing bulk. This results in the generation of a very thin zone within which intermolecular friction is greatly reduced. Figure 1-4 is a sketch of this phenomenon showing: (a) the flow of a polymer over a flat surface in the presence of strong polymer adsorption represented by thick chains and interfacial chain entanglements; (b) the adsorbed chains are gradually disentangling from those in the bulk when $\sigma > \sigma_c$.

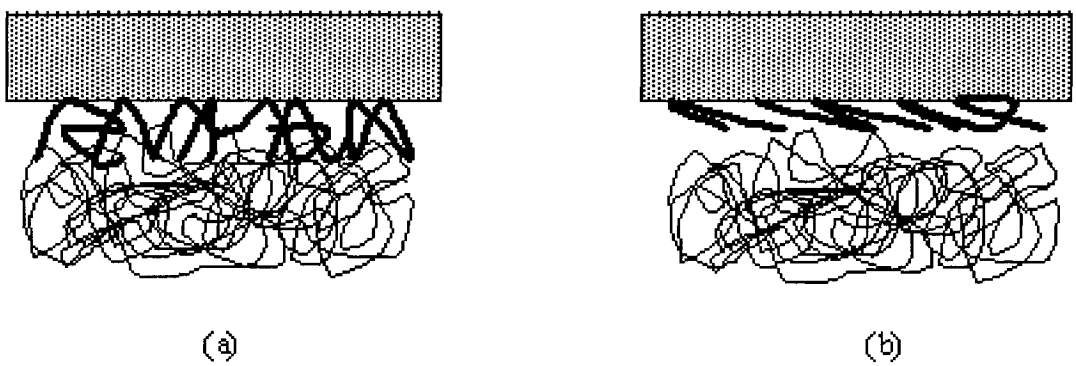

Figure 1-4 Polymer disentangles from a steel surface: (a) no slip; b) slip starts.

It is now believed that the factors influencing slip include the chemical nature of the polymer, its molecular weight and distribution, branching structure, entanglement density of the bulk polymer, the topography of the polymer-wall interface, the surface energy of the wall materials, temperature, and flow conditions.

1.6 Scope and Objectives

The sliding plate rheometer developed at McGill has significant advantages over other types of rheometers when studying the NLVE behavior of polymer melts. This instrument is capable of detecting shear and normal stresses locally and directly in a uniform shearing deformation. It thus made possible for the first time reliable transient stress measurements for large, rapid shearing deformations of polymer melts.

The detailed objectives of the project were to:

1. Develop experimental techniques for making reliable measurements of shear stress during large transient shear flows using a modified shear stress transducer.
2. Evaluate a proposed method for measuring the first normal stress difference using a normal stress transducer.
3. Compare transient and steady-state shear responses with predictions of the Wagner constitutive equation in order to determine the slip behavior for these situations.
4. Compare the types of slip behavior occurring on steel and glass.
5. Measure stress responses in step strain stress relaxation and verify the time-strain factorability of the nonlinear relaxation modulus.

Chapter 2 Methodology

2.1 Polymers Studied

2.1.1 Selection

Since the objective of this study is to examine nonlinear viscoelasticity, polymers were selected on the basis of their exhibiting a strong nonlinear response when subjected to large, rapid transient shear deformations. It was also necessary to choose polymers, the behaviour of which could be predicted using existing rheological models, meaning that they must be linear, monodisperse, and highly entangled. The polymer used was polybutadiene (PBd) synthesized in the laboratories of the Firestone Tire and Rubber Company; this polymer has the following chemical structure:

$$-\left(CH_2 - CH = CH - CH_2\right)_n -$$

This polymer is amorphous and has a glass transition temperature of -90 °C. Two PBd samples having low polydispersities and different molecular weights were studied. The entanglement molecule weight (M_e) of PBd is small (≅2000) compared to that of most other polymers, and the requirement of a high level of entanglement (M_w/M_e) is satisfied. The structural properties of these two polymers are shown in Table 2-1. Vinogradov [15] found that PBd exhibited the spurt effect in capillary flow only when M/M_e was greater than about fifty.

Table 2-1 Characteristics of PBd Samples

Sample No.	PBd 2	PBd 3
Producer	Dr. Christopher Robertson	Dr. Mark DeDecker
Composition	rich in 1,4 addition (91mol%)	rich in 1,4 addition (90%)
Grade	2622-114	SR-8726
M_w	78,000	194,000
PDI (M_w/M_n)	1.04	1.06
Entanglement Density M/M_e (N/N_e)	50	130
	N_e is average number of monomers between entanglements	

2.1.2 Preparation

Monodispersed PBd is generally synthesized by anionic polymerization of 1,3-butadiene in hexane using s-butyl lithium as an initiator. The reaction was carried out in a 19 liter lab-scale batch reactor at 55-60°C for 1.5 hours. The living polymer-lithium cement was discharged from the reactor into isopropanol to terminate polymerization and serve as a coagulation step. A small amount (1000 ppm relative to polymer weight) of BHT antioxidant was added to the isopropanol prior to termination / coagulation to help protect the subsequently isolated and dried polymer from thermal-oxidative attack.

Chemical characterization was carried out in the Firestone laboratories. The microstructure was analyzed using ^{1}H and ^{13}C NMR with a deuterated chloroform solvent. The glass transition temperature, T_g, was measured by differential scanning calorimetry at a heating rate of 5°C/min after cooling at the same rate. Gel permeation chromatography (GPC) was performed in THF using a Waters Model 150-C with a refractive index detector. GPC measurements were conducted relative to polystyrene standards, and the results were then converted to absolute molecular weight by applying the universal calibration approach using data concerning the molecular weight dependence of intrinsic viscosity.

All rheological tests and molding processes for the putty-like PBd2 were conducted at 50°C, while those for rubber-like PBd3 were conducted at 100°C. Sliced samples were molded into rectangular plaques, 1 mm thick, between stainless steel plates with shallow grooves along the transverse direction, using a Carver Press model 2114. Venting was required before the set temperature became constant to repel air trapped inside the sample. The mould was held under a pressure of 20 tons at the set temperature for two hours. The pressure was then maintained overnight, during which time the sample was allowed to air-cool to room temperature.

2.2 Apparatus

2.2.1 Stress-Controlled Rheometer

Before making LVE measurements, the thermal stability and useable lifetime of the samples were determined by means of a time sweep using a Rheometric SR5000 stress-controlled rheometer (Figure 2-1). In the SR5000, stress is applied by the stress head, which consists of a motor and an air bearing. When a sample is loaded between two parallel plates of 25mm diameter, the applied torque will induce a deformation, which is determined from the angular displacement of the bearing as measured by the position tensor. Using the geometric factors for the plates, the stress and strain can then be computed.

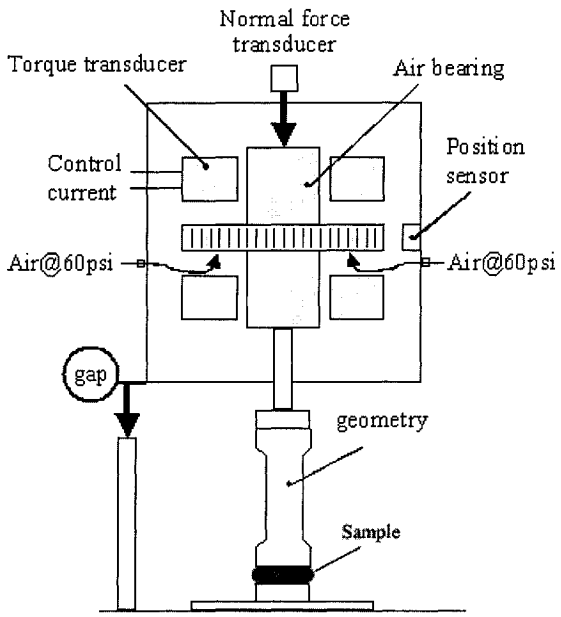

Figure 2-1 Schematic diagram of SR5000.

In a time-sweep experiment, the sample is subjected to an oscillating stress at fixed amplitude, frequency and temperature, and the strain is recorded. All measurements were made with the sample in a nitrogen atmosphere. The frequency selected should be neither too low, which would require a long time and degrade the polymer, nor too high, which would result in errors due to instrument compliance. A frequency of 1 rad/*s*was selected. The strain should be within the linear deformation limit for the sample at the chosen frequencies, but should not be so small as to lead to loss of precision in the output of the strain transducer.

2.2.2 Strain-Controlled Rheometer

The LVE measurements were performed using an Advanced Rheometric Expansion System (ARES), which is a strain-controlled rheometer (Figure 2-2) made by Rheometric Scientific (now TA Instruments, Inc.). This instrument is capable of subjecting a sample to a dynamic shear strain and measuring the resultant torque in the sample in response to the strain. The torque transducer has a maximum torque of 500 g-cm.

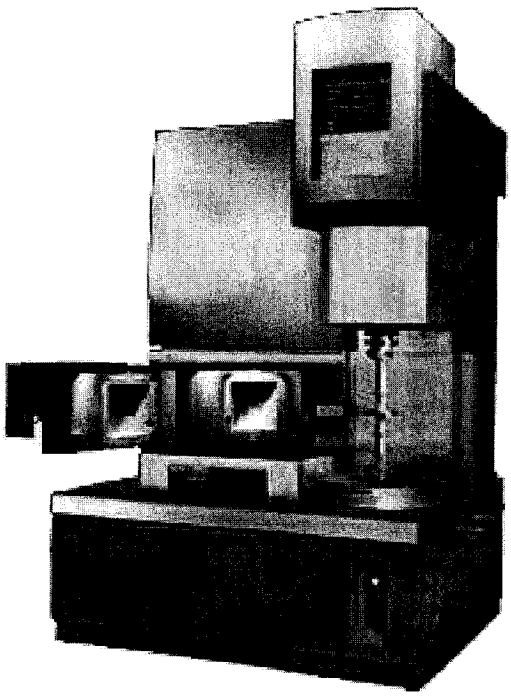

Figure 2-2 ARES Test Station.

Frequency sweep tests were performed to determine the storage and loss moduli: $G'(\omega)$, and $G''(\omega)$, which were used to calculate the continuous spectrum $H(\lambda)$. The results are presented in Chapter 3. The heating medium in the forced-convection oven was nitrogen.

2.2.3 Sliding Plate Rheometer

2.2.3.1 Limitations of Pressure Flow and Rotational Rheometers

To study nonlinearity, it is necessary to subject the material to a large, rapid strain in which the strain is uniform throughout the sample and precisely controlled as a function of time. In order to generate a uniform transient flow and obtain data that can be interpreted in terms of well-defined material functions, it is desirable that flow generated by the rheometer be as close as possible to simple shear flow. This can be accomplished by the use of a drag flow involving either rotational or rectilinear motion of a solid surface. Rheometers based on rectilinear motion are referred to as sliding surface rheometers.

While capillary rheometers are popular because of their simplicity and ease of use, they provide information only about the shear stress associated with steady shear. Thus, they are used primarily for the measurement of viscosity at high shear rates. Thus, capillary rheometers are capable of generating high shear rates, but the non-uniform strain field makes it impossible to study time-dependent rheological phenomena such as viscoelasticity using a pressure-driven flow. Rotational rheometers can generate deformations in which the strain is essentially uniform, but they are limited to use at quite low strain rates due to various flow instabilities [16,17], for example, viscous heating produces temperature gradients and variations with time; end and edge effect causes severe distortion of the free surface [16,18]. Some of these limitations can be overcome by using instruments that employ rectilinear flows with uniform shear; *i.e.*, by using sliding plate rheometer (SPR). And by measuring the shear stress locally, by use of a shear stress transducer, edge effects are not a problem.

2.2.3.2 Design Features

A sliding plate rheometer (SPR) equipped with either a shear stress transducer (SST) or a normal stress transducer (NST) was used. This instrument was developed by Giacomin and Dealy [19,20,21,22] and has been used in the past to study the behaviour of concentrated solutions at room temperature [23,24] and molten plastics [20,25,26]. Figure 2-3 is a side view showing the essential features of the SPR.

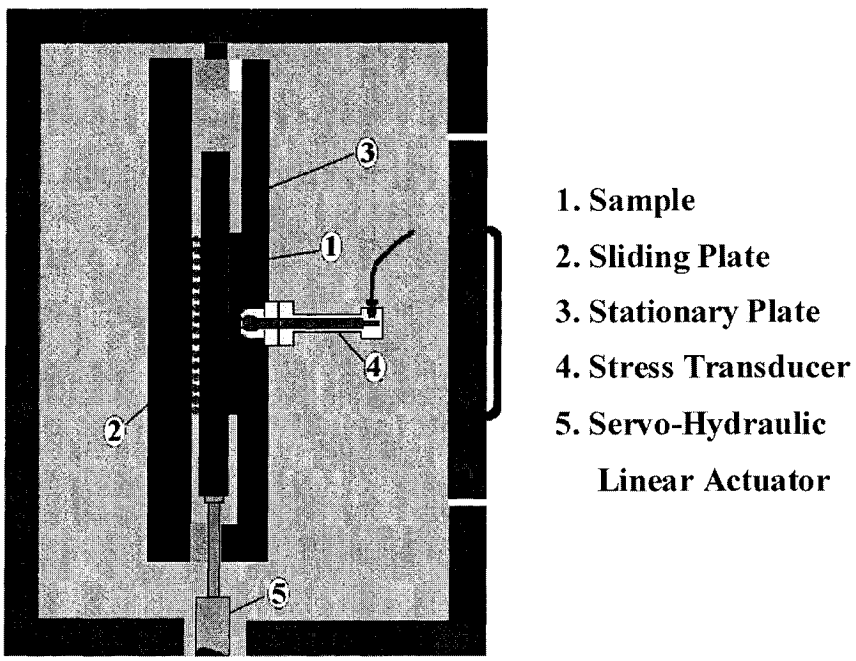

Figure 2-3 Sideview of SPR incorporating a SST.

The sample (1) is sheared between the moving plate (2) and the stationary plate (3). A precision linear bearing table is used to support the moving plate. The displacement of the moving plate is driven by a servo-hydraulic linear actuator (5), which can be programmed to generate a wide range of shear histories involving shear rates from 10^{-3} to 800 s^{-1}. The stress transducer (4) is mounted on the fixed plate (3). An LVDT provides the feedback signal for a control loop that regulates the actuator position. The SPR can be operated in either strain-controlled or stress-controlled modes.

The shear strain γ is the displacement X of the moving plate divided by the distance h between the plates:

$$\gamma = X / h \qquad (2\text{-}1)$$

The shear rate $\dot{\gamma}$ is then the velocity V of the moving plate divided by the gap:

$$\dot{\gamma} \equiv V / h \tag{2-2}$$

In older In older sliding-plate instruments the shear stress σ was inferred from the force F required to drive the motion of the moving plate (or the force required to hold the stationary plate in place) and the area A, of the sample in contact with one plate:

$$\sigma = F / A \tag{2-3}$$

However, many of the possible sources of error stated in Section 2.2.3.1 can be eliminated or greatly reduced if the stress is measured locally using a shear stress transducer at the center of the sample, rather than being inferred from the total driving force. This is especially advantageous in studies of the nonlinear response of viscoelastic materials. Figure 2-4 shows a shear stress transducer developed by Dealy [22,27].

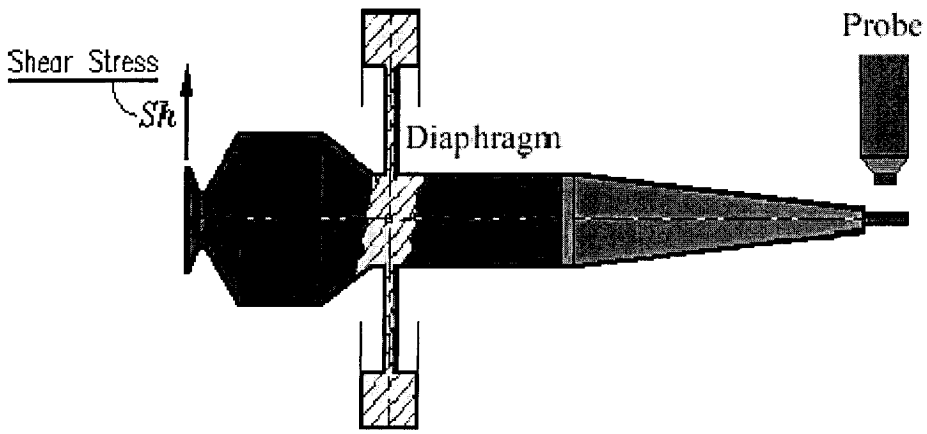

Figure 2-4 Diaphragm Shear Stress Transducer

The active face at the end of a rigid beam is flush with the surface of the fixed plate. This rigid beam is supported by a steel diaphragm, which provides the restoring force. The beam deflects in response to shear forces acting on the active face in contact with the sample. The deflection of the beam is detected by a capacitance-type proximity probe (Capacitec), while the end of the probe and surface of the beam act as the plates of a capacitor. The associated circuitry produces an output voltage proportional to the distance between these plates, which in turn is proportional to the deflection of the beam.

In addition to the shear stress detected by SST, another rheologically meaningful quantity that can be determined by SPR system is the first normal stress difference N_1. This quantity is sensitive to the nonlinear viscoelasticity of a polymer. It was detected by a normal stress transducer (NST) built into a special stationery plate (Figure 2-5). The free ends of the sample are exposed to the atmosphere, $\sigma_{11} = 1\ atm$, and $N_1 \approx -\sigma_{22}$ [28]. A direct measurement of $-\sigma_{22}$ is made by placing a hole in the back of the fixed plate and leaving a thin diaphragm of steel in contact with the sample. The diaphragm has a diameter of 10 mm and a thickness of 0.6 mm. The deflection of this diaphragm in response to a normal stress is detected by a capacitance probe. The maximum pressure of 500 psi results in a diaphragm deflection of 10-11 mm.

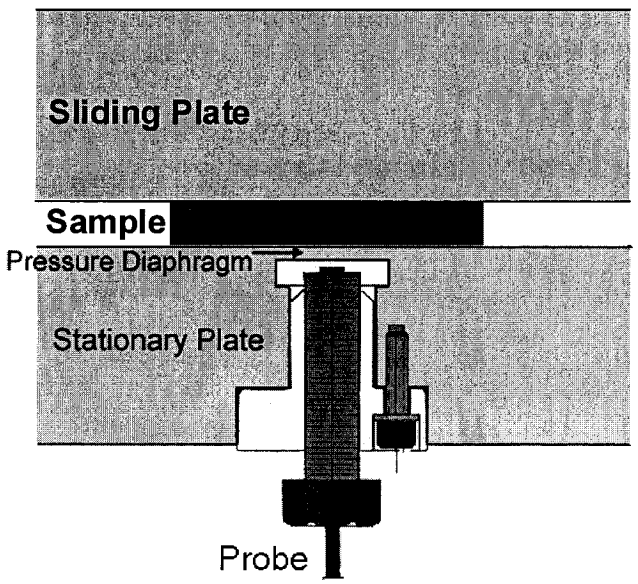

Figure 2-5 Special stationary plate adapter for normal stress transducer.

2.2.3.3 Advantages and Modifications for Disadvantages

A sliding plate rheometer incorporating stress transducers has significant advantages over other types of rheometer for generating large, rapid shear deformations. It is thus ideal for studying nonlinear viscoelasticity in polymer melts. In the SPR, the shearing motion is generated by a servo-hydraulic linear actuator that can be programmed to generate a wide range of shear histories involving total strains of up to 400, at shear

rates of up to 800 s^{-1}. The most critical feature of SPR is the stress transducer. This device makes it possible to measure shear stress locally over a small area in the center of the sample so that it is not necessary to infer the stress from the total shear force on one plate. This eliminates errors arising from end and edge effects as well as instrumental friction. Over an extended period of time, changes in the sample occurring at its free surface, such as oxidation and absorption of moisture, have a minimal effect on the stress and strain in the neighbourhood of the stress transducer. By contrast, in a rotational rheometer, the free surface where degradation and composition first occur is at the outer rim, which has the maximum effect on the measured torque.

Effect of gap size

Several sources of error in the SPR can be detected by varying the gap h. In particular, wall slip can be detected by looking for a gap-dependence in the shear stress for a given plate speed (as explained in Section 2.3). To minimize other errors, such as shear waves and temperature non-uniformity, it is advantageous to use small gaps. This also maximises the total shear strain and nominal shear rate defined by Eqs. 2-1 and 2-2.

Diaphragm-dependent stress limit

The limits of shear stress and normal stress sensed by the SST and NST are both governed by the stiffness of diaphragm. The diaphragm for the NST has a maximum pressure limit of 500 psi, or about 3440 KPa, which provides a broad measurement range. For the SST, a 1.35 mm disk-spring provides a 300 KPa limit on shear stress, which provides good sensitivity for moderate stresses but is too compliant for high stresses. In order to make reliable NLVE measurements with the PBds in question, a SST with a 1.7 mm disk-spring was made. The thicker diaphragm has a maximum stress of 600 KPa.

Secondary flow and prevention

Since the sample is always of finite size, and its edges and ends are exposed to air at ambient pressure, there are gradients in the normal stresses from the ends and edges of the sample to the center, and these provide the driving force for a flow that draws melt in from the ends and pumps it out at the edges [23, 29] (Figure 2.6). This secondary flow

relieves normal stresses and prevents the establishment of true simple shear flow. I have found that this undesired component of the flow can be suppressed by placing rods of solid fluorocarbon in rails that are machined into the plates, as shown in Figure 2-6.

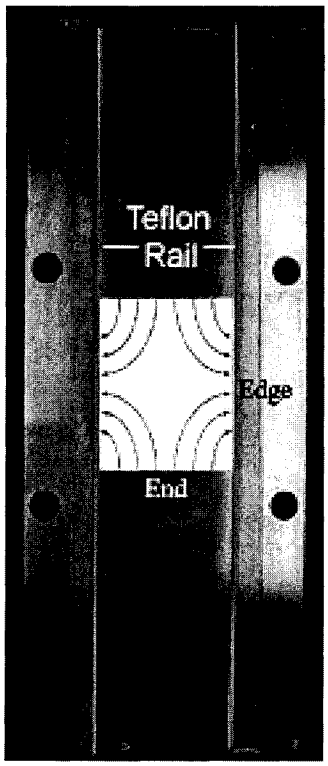

Figure 2-6 Secondary flow in SPR moving plate and Teflon side rails for prevention

Damping effect in SST

In order for the beam to be able to deflect in response to the shear force exerted by the melt on the active face, there must be a small gap separating its periphery from the circular hole in the fixed plate in which it is mounted. To ensure that the sample uniformly wets both plates, it must be slightly thicker than the final gap between the plates. As shown in Figure 2-7, when the sample is squeezed between the two plates, some polymer flows into the transducer housing through the gap between the edge of active face and the rim of the hole in the fixed plate, and this dampens the dynamic response of the transducer. The end of the beam is designed to minimize this damping, but some attenuation and phase shift are inevitable.

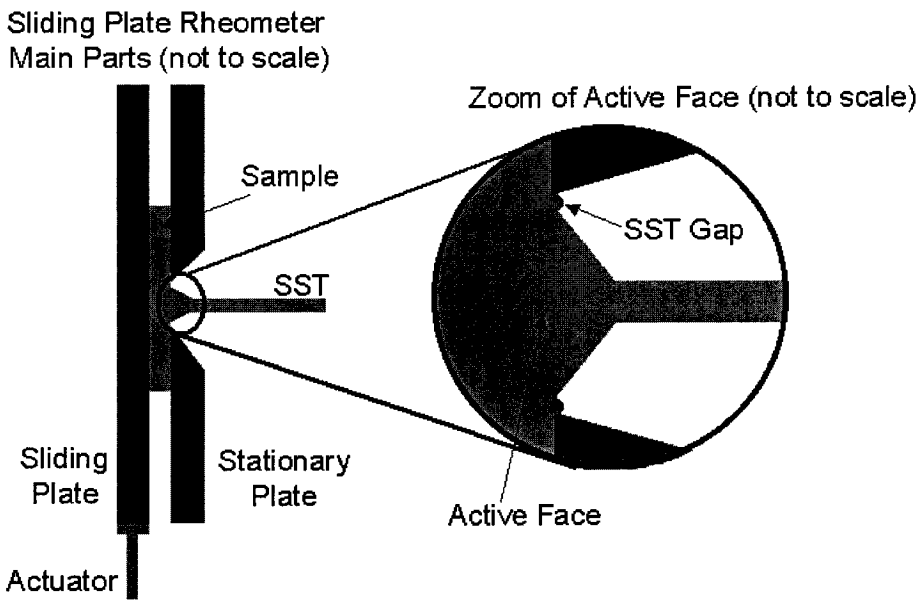

Figure 2-7 Schematic of damping effect.

The current design is based on an analysis of the forces acting on the beam (Eq. 2-4 and Figure 2-8).

$$L_c \cdot F_{spring} = M_{beam} + L_f \cdot F_{polymer-in-gap}$$

$$\text{where } F_{polymer-in-gap} = C \int_0^t \sum_{i=1}^{n} G_i \exp[-(t-t')/\lambda_i] d[b(t')] \qquad (2\text{-}4)$$

where G_i, λ_i are the parameters of a discrete relaxation spectrum for the sample; $b(t')$ is the SST gap size; C is a proportional constant; L_f is the moment arm of the shear force F_p; and L_c is the moment arm of the spring force F_s.

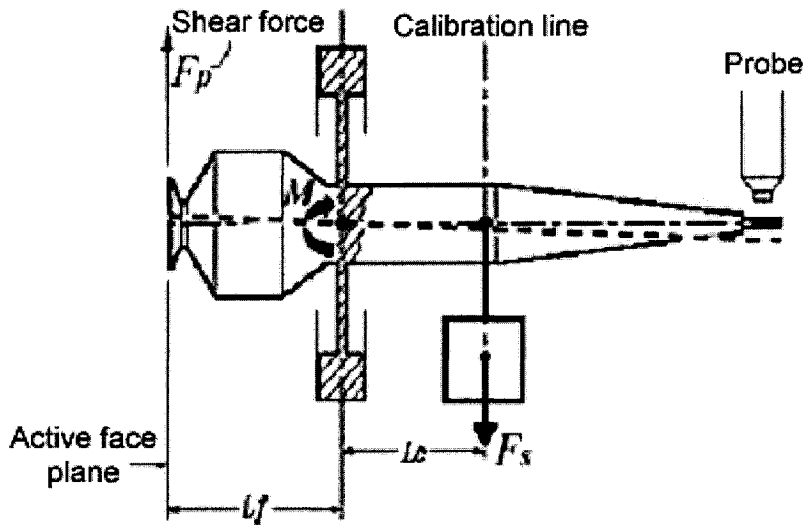

Figure 2-8 Mechanical analysis of SST beam.

This model reveals that the principal contribution to damping is the force due to compression and tension imposed at the end of beam, which is inversely proportional to the cube of the gap size b_0. Therefore, as b_0 increases, the magnitude of the damping decreases significantly. However, if b_0 increases further, it is possible that the large gap will disturb the shear flow between the plates. It was decided to decrease the active face diameter from 10 mm to 9.90 mm, where the b_0 was increased from 0.04 mm to 0.09 mm. This change was expected to decrease the damping while causing minimum disturbance to the flow. The damping effect is particularly significant when the melt is subjected to rapid transient shear flows. Thus, it is essential to evaluate the extent of the damping by performing a ramp displacement experiment.

Figure 2-9 shows the gap distance as a function of time for a fairly high ramp rate. We see that the magnitude of the damping is less than 1.5%, implying an acceptable design of the active face of the SST and verifying that the model is able to describe quantitatively the damping effect.

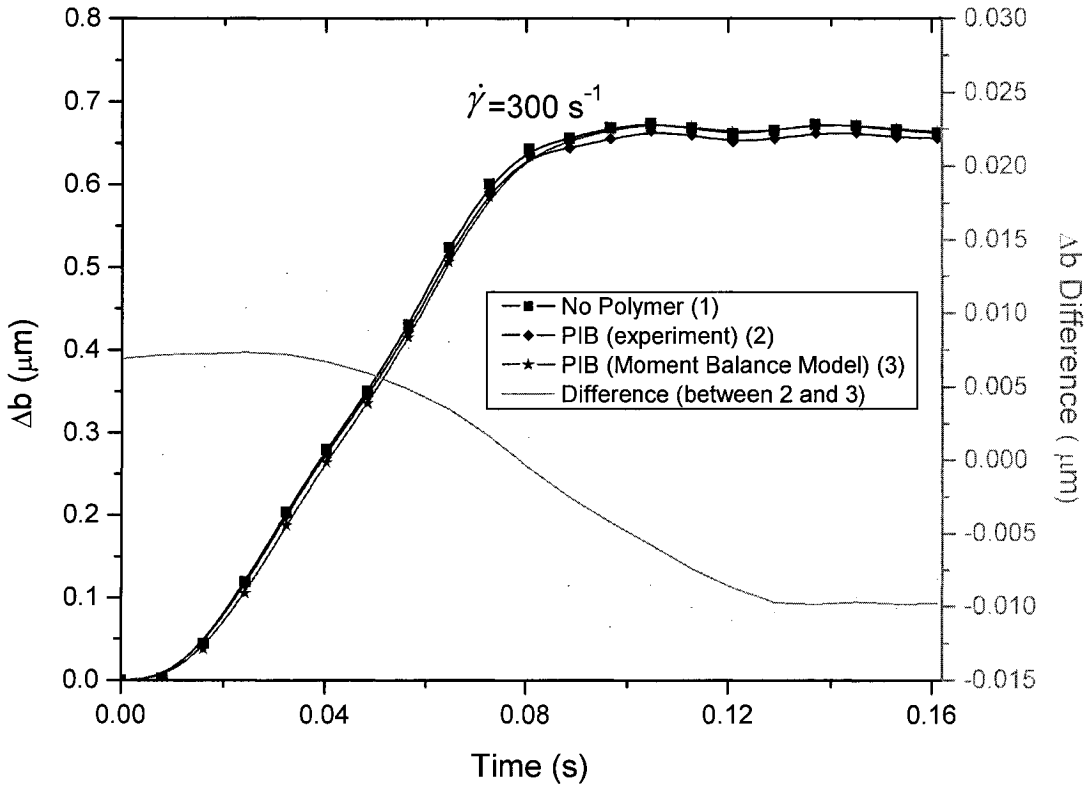

Figure 2-9 Effect of design change on damping in SST.

2.3 Wall Slip Determination

The shear stress is measured at various nominal shear rates $\dot{\gamma}_n \equiv V/h$. Since this is not equal to the true shear rate corresponding to the measured stress, in order to determine the slip velocity, it is necessary to know the viscosity as a function of shear rate under no-slip conditions. The true viscosity curve was estimated by use of the "Cox-Merz rule" (Eq. 2-5). As observed by Cox and Merz [30], the curves of $\eta_A(\dot{\gamma}_A)$ (apparent viscosity versus apparent wall shear rate) are often nearly identical to curves of $|\eta^*|$ versus ω.

$$\eta_A(\dot{\gamma}_A) = |\eta^*(\omega = \dot{\gamma})| \tag{2-5}$$

The complex viscosity as a function of frequency was obtained using a rotational rheometer ARES (Section 2.2.2). In order to obtain the viscosity as a function of the true shear rate, it is necessary to shift the function shown on the left. This can be done using the Rabinovitch correction, but a more convenient procedure is the Schümmer approximation [31], which gives:

$$\eta(0.83\dot{\gamma}) = \eta_A(\dot{\gamma}_A) \tag{2-6}$$

Thus, to obtain the viscosity function, it is only necessary to shift the curve by 0.83. Combining Eqs. 2-5 and 2-6, we obtain:

$$\eta(0.83\dot{\gamma}) = \eta_A(\dot{\gamma}_A) = |\eta^*(\omega = \dot{\gamma})| \tag{2-7}$$

The no-slip stress curve can thus be obtained from the corrected viscosity function given by Eq. 2-7.

Sliding plate geometry is the simplest drag flow rheometer in use to study wall slip. The basic principle is shown in Figure 1-3. Here, the nominal shear rate is the speed of the moving plate, V, divided by h, the gap separating two plates:

$$\dot{\gamma}_n \equiv V/h \tag{2-8}$$

When slip occurs, the true (no-slip) shear rate $\dot{\gamma}$ is no longer the quantity given by Eq. 2-3 but is related to $\dot{\gamma}_n$ as follows:

$$\dot{\gamma} = \frac{V}{h} - \frac{V_1}{h} - \frac{V_2}{h} = \dot{\gamma}_n - \frac{V_1}{h} - \frac{V_2}{h} \tag{2-9}$$

where V_1 is the slip velocity on plate 1, and V_2 is the slip velocity on plate 2. If slip occurs at both plates at the same velocity V_s, we have:

$$\dot{\gamma} = \frac{V}{h} - \frac{2V_s}{h} \tag{2-10}$$

Measurements in the SPR are normally made using two steel plates. To study slip on other substrates, the material of construction of the moving plate can be changed, while the fixed plate must be of stainless steel if the shear stress is to be measured, to provide for the mounting of the SST.

Figure 2-10 is a sketch showing the behavior of flow curves with and without slip, as measured in the SPR. The uppermost line is the no-slip curve obtained from complex viscosity data together with the Cox–Merz rule. The middle curve shows a typical stress response with slip behavior on stainless steel, and the lowest curve shows the behavior of a melt flowing over a low-energy surface, such as one coated with a fluorocarbon. In this case, the density of adsorbed sites is much less, and the friction between adsorbed and bulk molecules is thus greatly reduced, leading to enhanced slip.

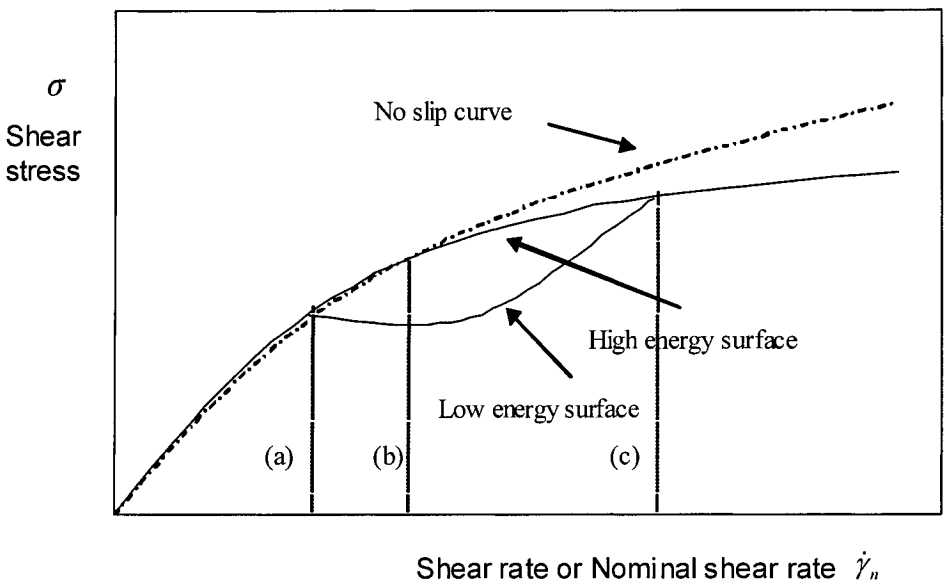

Figure 2-10 Effect of slip on SPR flow curve (Sketch based on data of [9]).

In Fig. 2-10, for a given steady-state shear stress σ the no-slip shear rate $\dot{\gamma}$ is given by the top curve, while the nominal shear rate $\dot{\gamma}_n$ at the same stress for steel plates is given by the middle curve. The slip velocity for the high-energy steel substrate V_{st} as a function of shear stress can then be calculated using Eq. 2-10.

Similarly, for a glass moving plate and a steel fixed plate, the slip velocity on the glass plate V_g can be calculated from the known V_{st} at the same stress from the steel-steel measurement:

$$\dot{\gamma} = \dot{\gamma}_n - \frac{V_{st}}{h} - \frac{V_g}{h} \tag{2-11}$$

Moreover, by analogy with Eq. 2-10, the true shear rate for a glass/glass SPR experiment can be written in terms of V_g:

$$\dot{\gamma} = \dot{\gamma}_n - \frac{2V_g}{h} \tag{2-12}$$

Subsequently, the shear stress for a glass/glass setup can be calculated using the true shear rate given by Eq. 2-12 together with the no-slip stress curve.

2.4 Calibration of Stress Transducers

2.4.1 Calibration of Shear Stress Transducer

The calibration of the stress transducers is carried out at the measurement temperature. Figure 2-11 shows the calibration assembly for the shear stress transducer. A steel wire is attached to the beam of the SST at one end with a weight hung from the other, which simulates a shear force acting on the active face of the SST. By varying the load and measuring the SST response, the linearity of the output is verified, and the calibration constant is determined. The SST is equipped with a precision positioning system that makes it possible to set the initial gap between the capacitance probe and the beam to give a zero SST output. The voltage output is compared with the simulated stress in Figure 2-12.

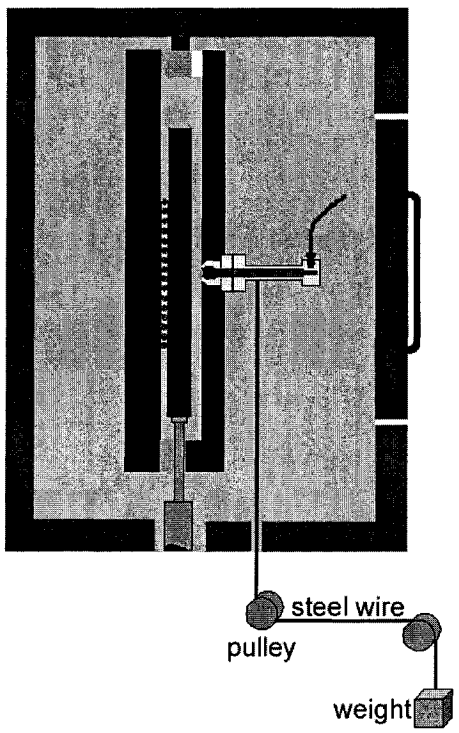

Figure 2-11 Calibration assembly for SST

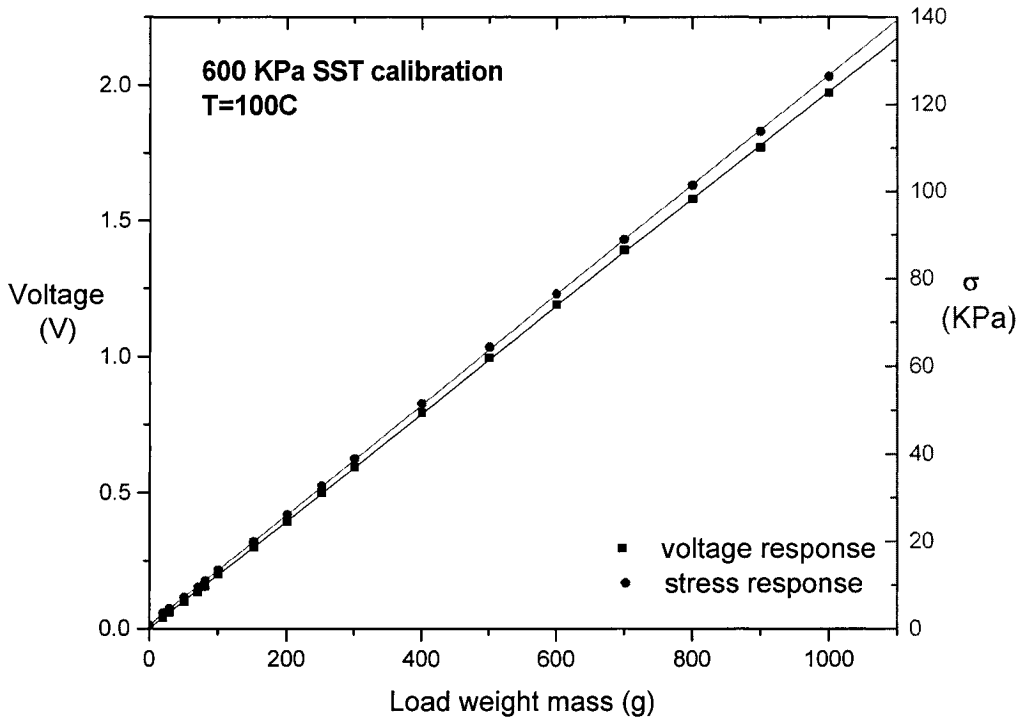

Figure 2-12 Shear force calibration of SST.

2.4.2 Calibration of Normal Stress Transducer

A removable calibrating system was designed to allow the calibration of the normal pressure transducer (NST) inside the oven at operating temperature. This system is shown in Fig. 2-13 and consists of a pressure plate and a calibrating bridge. During calibration, the bridge clamps together the SPR fixed plate, the pressure plate and the moving plate by means of four bolts fastened directly into the rheometer base frame. The linearity of the capacitance probe output voltage with the applied pressure can be seen in Fig. 2-14.

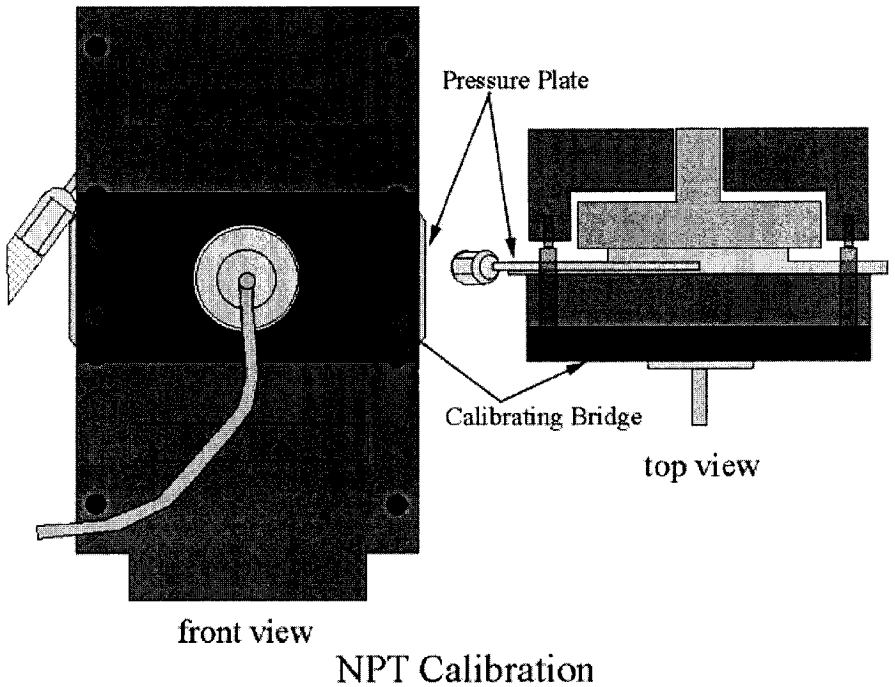

Figure 2-13 Calibration system for NST

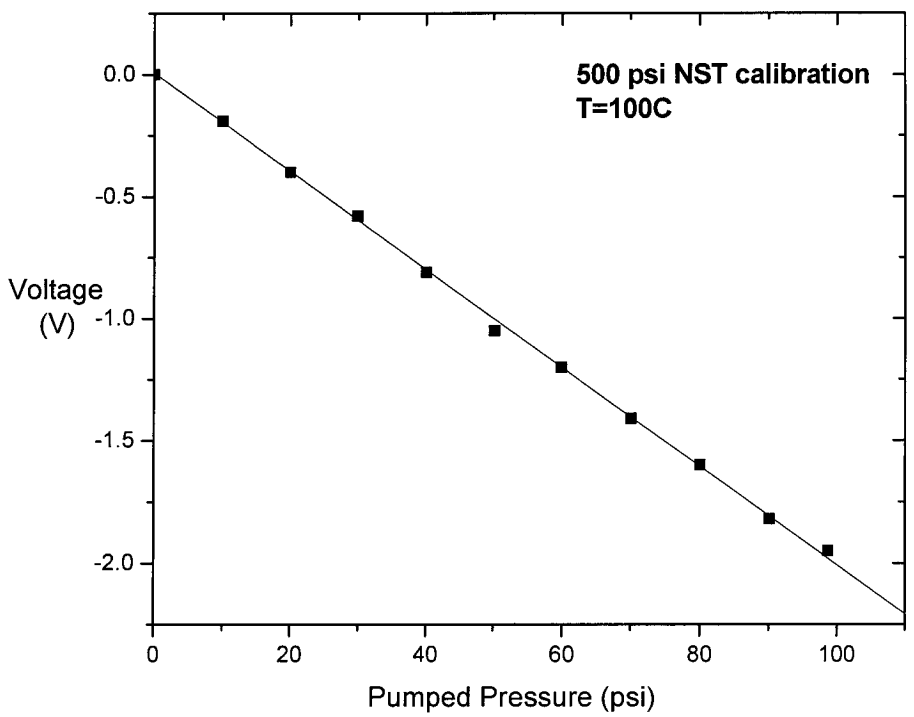

Figure 2-14 Normal force calibration of NST

2.5 Nonlinear Viscoelasticity Experiments

The two nonlinear viscoelasticity experiments carried out were stress relaxation after a large step strain and start-up of steady simple shear. The WinTest system provided by EnduroTec, Inc. was used to control the experiments and acquire data.

After the sample was loaded and the set temperature was reached, a small-amplitude oscillatory pre-shear was applied to press the sample against the side rails on the moving plate so that secondary flow would be suppressed. Figures 2-15 shows the loaded sample before oscillatory pre-shear (left) and after pre-shear (right).

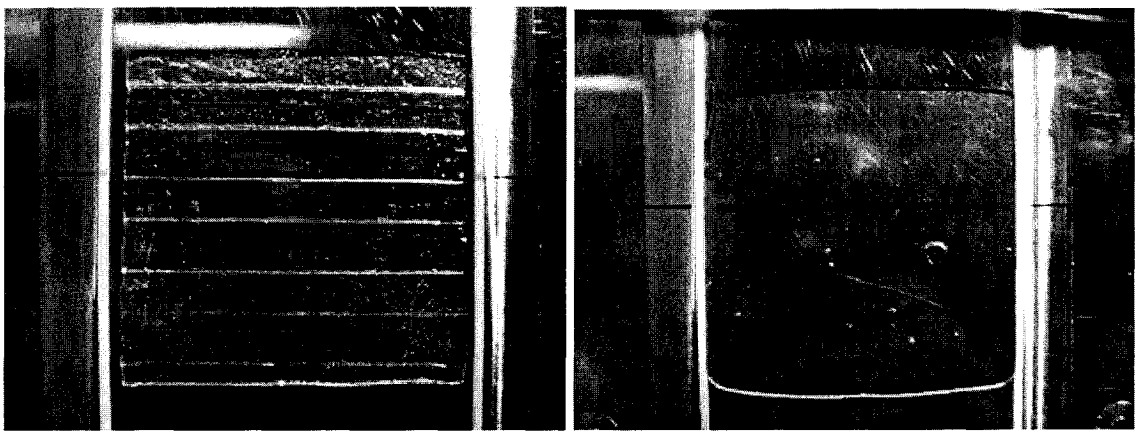

Figure 2-15 The appearance of the sample before oscillatory pre-shear (left) and after pre-shear (right). (As revealed by the use of a glass stationary plate.)

Monitoring the normal stress as a function of time after starting the deformation provides information concerning the time required for the stresses resulting from one test to relax so that the next test could be started. It was found that one-hour of rest time was generally required between shear deformations. For each test condition, at least three experiments with different samples were carried out under the same conditions. The run-to-run variation, which reveals the reproducibility of the experimental data, was less than 3%. Considering experimental uncertainty, 3% was deemed an acceptable value. The temperature variation during an experiment was ±0.3 °C.

For start-up of steady simple shear a ramp command to the actuator was generated by Wintest. To avoid the premature breakage of samples, a sequence of tests always started with the smallest or slowest deformation and progressed to higher magnitudes or

rates. Due to limitations of the control system, the true time at which actuator motions started was 0.02 seconds after the start time, as is shown in Fig. 2-16. Thus in reporting data, the time scale is shifted by 0.02 seconds so that $t = 0$ corresponds to the time the plate actually started to move.

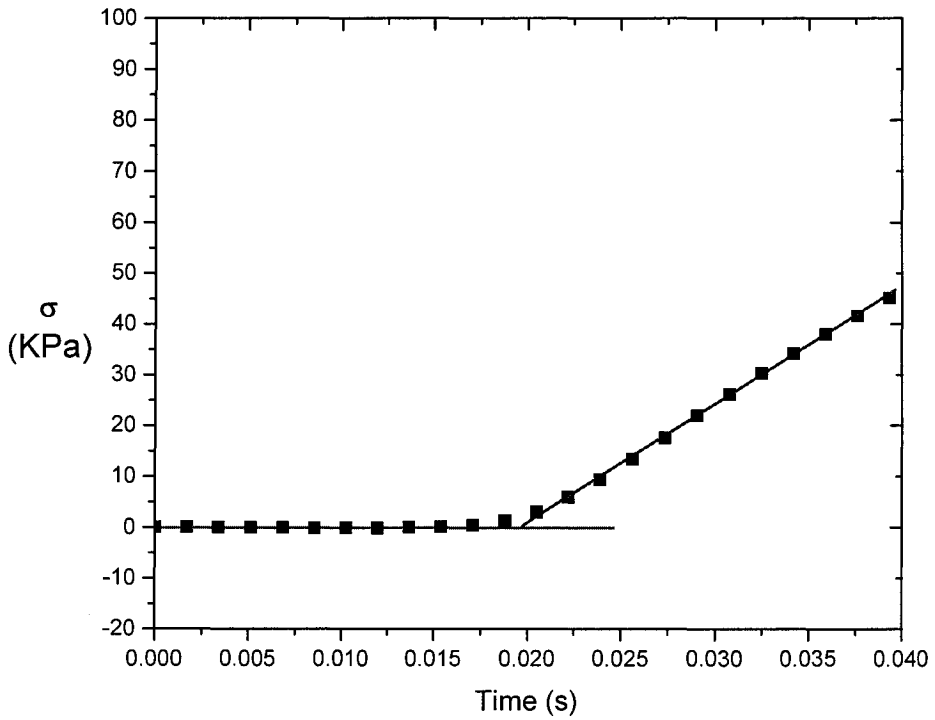

Figure 2-16 The effect of inertia characteristics on stress response in a transient time.

A true step strain deformation is impossible to generate in practice, as it requires the instantaneous displacement of a shearing surface. The actual experimental displacement was a very high-speed ramp up to the desired strain by means of a square-wave. The actual ramp speed depends on the dynamic response of the control system and the servo-hydraulic actuator. Figure 2-17 compares the command signals and actual displacement for a programmed step and programmed ramps at two rates. The best response was obtained by using a ramp with a 800mm/s rate.

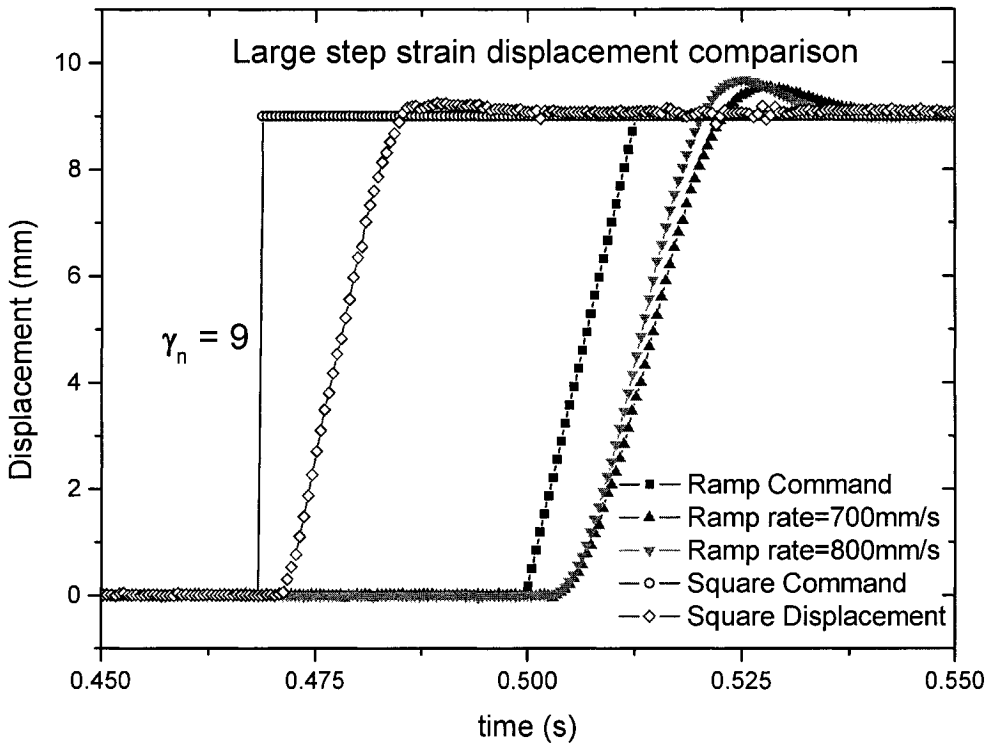

Figure 2-17 Large step strain displacement comparison.

The actual strain as a function of time depends on the mechanical characteristics and control system of the rheometer. Careful tuning of the controller parameters is thus required to optimize the system response. Typical strain and stress patterns are shown in Fig. 2-18. As in all "step-strain" experiments, there is a finite rise time Δt for the step to be completed and the stress to reach its maximum value. As a general rule, it has been found that data can be considered meaningful at times greater than $10\Delta t$ [32]. Another approach is to correct the data to take into account the non-zero rise time. Zapas [33] proposed that the independent variable, t, of the relaxation modulus can be calculated as follows:

$$t = t_0 - \Delta t/2 \tag{2-13}$$

where t_0 is measured from the instant that shear begins. In other words, the stress should be shifted left along the time axis by $\Delta t/2$. This procedure was used in the present study.

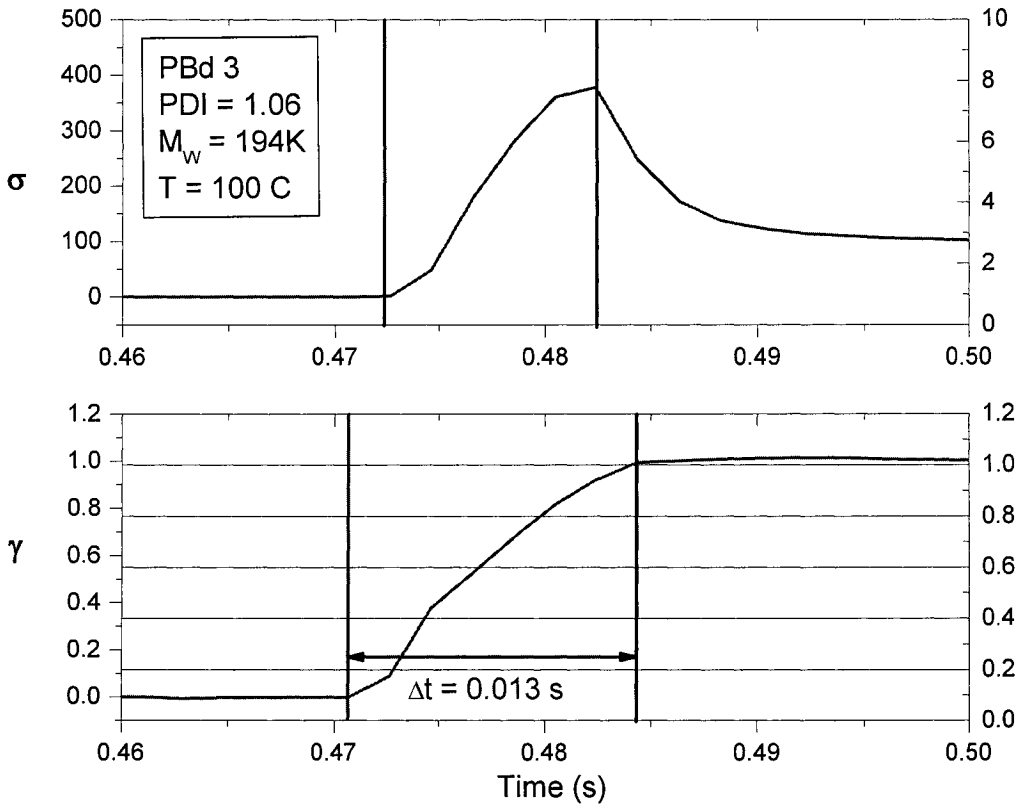

Figure 2-18 Strain and stress history at the rise stage of a step strain test.

Chapter 3 Results and Discussion

3.1 Thermal Stability of Samples

As explained in Section 2.2.1, a time sweep test is used to determine the effective lifetime of a sample. In principle, a sample is considered thermally stable if the change of $|\eta^*|$ from its the initial value (for linear samples) or its plateau value (for branched samples) is less than 3%. As seen from the Figures 3-1 and 3-2, the two samples behave very similarly and are stable for more than 15 hours with a variation in complex viscosity of less than 0.8%. Thus, all the viscoelasticity measurements were carried out within the period of thermal stability revealed by the time sweep tests.

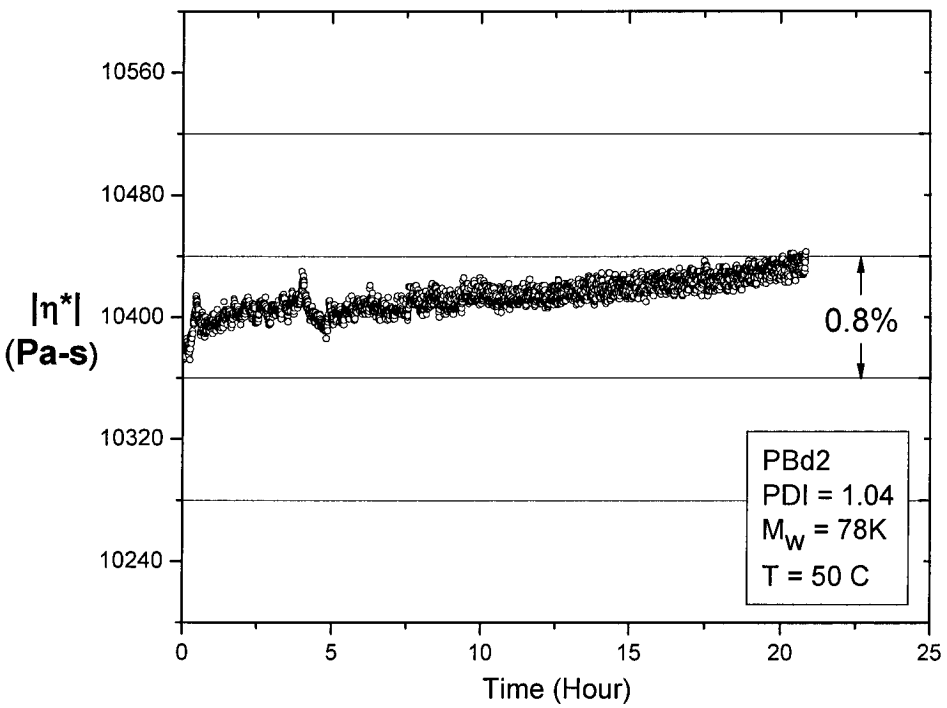

Figure 3-1 Dependency of |η*| on time for PBd2.

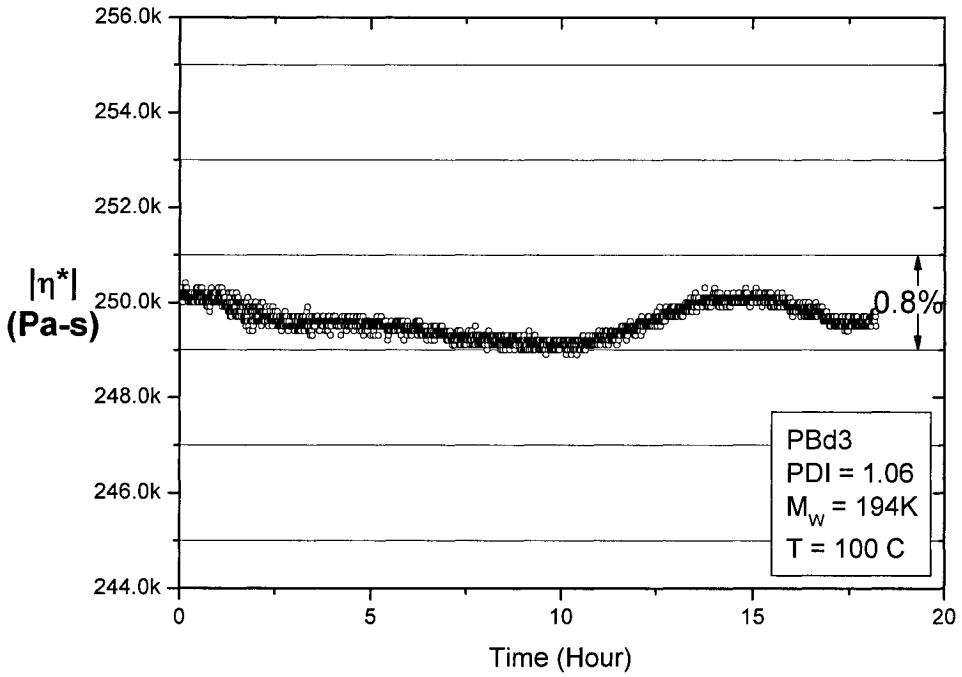

Figure 3-2 Dependency of |η*| on time for PBd3.

3.2 Linear Viscoelasticity

Results obtained using the ARES rheometer are presented in Figures 3-3 and 3-4. The points shown are averages of three runs, with a run-to-run variation of less than 1.2%. The complex modulus is used to obtain the no-slip viscosity function by use of Eq. 2-7. We see that the complex viscosity of both polymers exhibited a Newtonian plateau at the lowest frequencies, which was expected for these highly entangled, monodisperse materials. The storage and loss moduli were used to calculate the continuous relaxation spectra $H(\lambda)$ using the NLREG nonlinear regression software. The continuous spectra, which are shown in Figure 3-5, as well as the relaxation modulus $G(t)$ calculated from $H(\lambda)$ using Eq. 1-10 were used in the computation of all the linear and nonlinear viscoelastic properties using equations in Sections 1.2 and 1.3.

The reciprocal of the crossover frequency ω_c where $G' = G''$ provides a measure of the longest relaxation time, which should be of the same order as the disengagement

time τ_d of tube models. For PBd2, the crossover frequency is about 68 rad/s, implying a relaxation time on the order of 0.01 s. For PBd3, the crossover frequency is about 10 rad/s, indicating a relaxation time on the order of 0.1 s. It is not surprising that PBd3, having the higher entanglement density (Table 2-1), has a larger relaxation time.

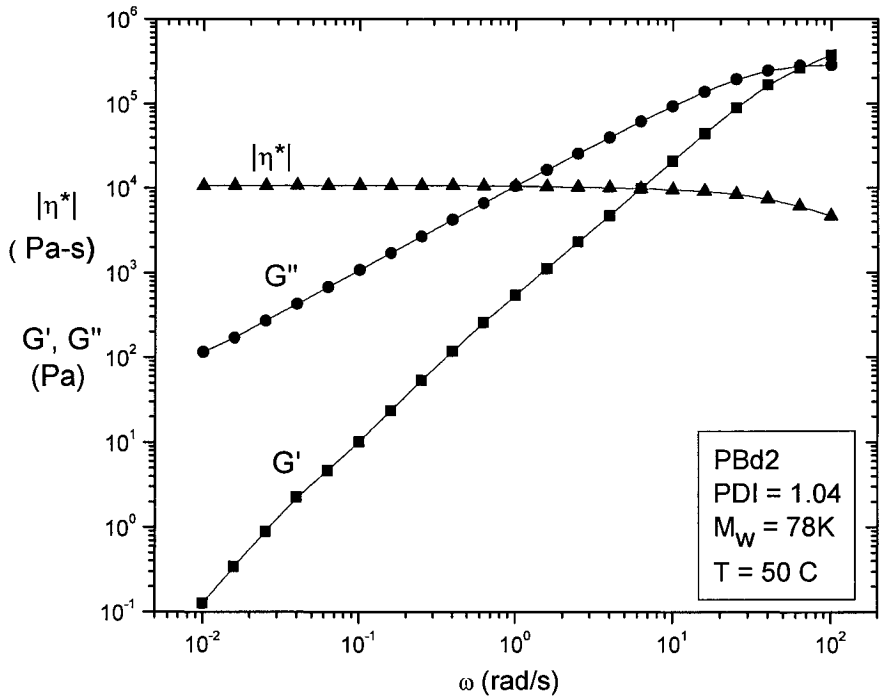

Figure 3-3 Dependency of |η*| and moduli on angular frequency ω for PBd2

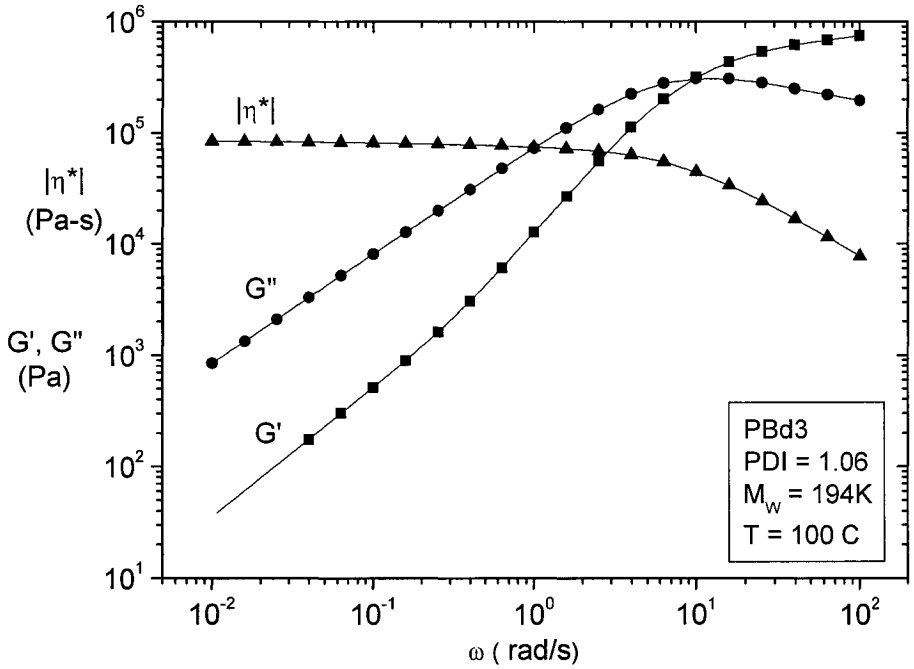

Figure 3-4 Dependency of |η*| and moduli on angular frequency ω for PBd3

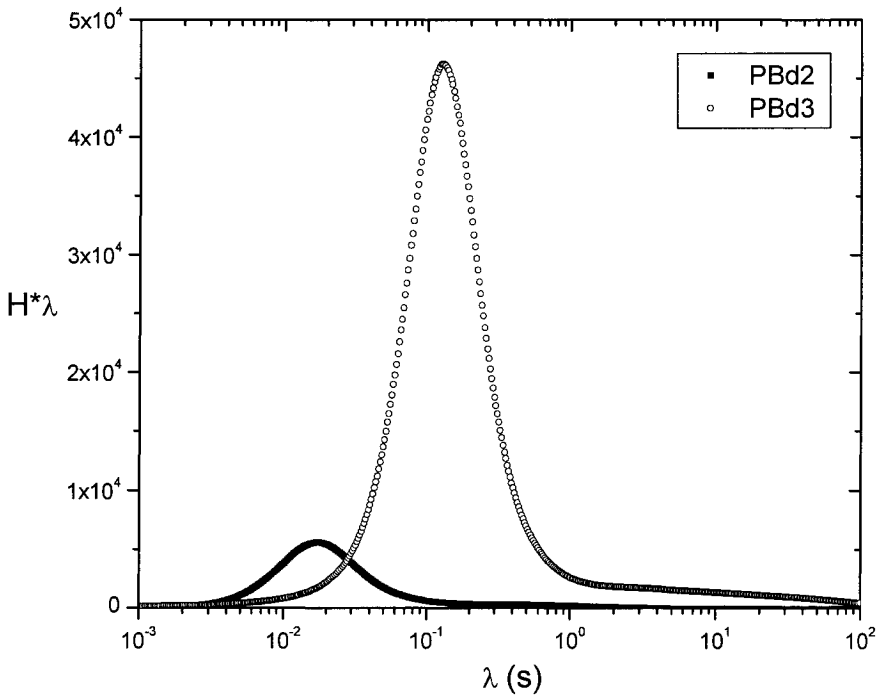

Figure 3-5 Time-weighted continuous relaxation spectra.

3.3 Start-up of Steady Simple Shear

3.3.1 Stress Growth Function and Transient Wall Slip

The stress was monitored as a function of time for start-up of steady simple shear. The shear stress start-up function defined by Eq. 1-33 is shown for several shear rates in Figs. 3-6 and 3-7. The upper envelope curve is the linear viscoelastic response calculated using Eq. 1-11. As the shear rate increases, the curves deviate from linear behaviour at progressively shorter times, exhibiting a stress overshoot followed by a steady state plateau, which gives the viscosity. Deviations from the linear curve at short times are caused by the limitations of the control system.

According to Eq. 1-43, the time to reach the maximum shear stress t_s should be inversely proportional to the shear rate. Plotting t_s as a function of $\dot{\gamma}$ (Fig. 3-8) we see that within experimental error t_s is indeed inversely proportional to $\dot{\gamma}$. The damping function parameter n is obtained by use of Eq. 1-43, and the predictions of the Wagner model for the nonlinear shear growth function, given by Eq. 1-41, are indicated in Figs. 3-6 and 3-7 by the solid lines.

Figures 3-6 and 3-7 compare experimental shear stress growth functions with predictions of Wagner's model. The predictions compare favourably with SPR responses at low shear rates, suggesting that no slip occurs at these rates. However, the stress falls increasingly below the Wagner predictions, and comes with slight undershoots as the shear rate increases, which implies that wall stick-slip is occurring, since slip causes the true shear rate to be smaller than the nominal shear rate (Eq.2-9). The actual shear rate $\dot{\gamma}(t)$ was estimated by dividing the measured stress by the Wagner model prediction for $\eta^+(t,\dot{\gamma})$, and this is related to slip velocity as shown by Eq. 2-10. The resulting slip velocity as a function of time for several nominal shear rates is shown in Figs. 3-9 and 3-10; this becomes constant when the steady state is reached. The steady-state slip velocity should be equal to the value inferred from the shear-rate dependent steady-state data presented in next section. It would be of more fundamental interest to carry out time-dependent slip experiments at constant stress rather than constant nominal shear rate, but

this would require the use of a feedback loop on stress that could lead to unstable actuator behavior and damage to the rheometer.

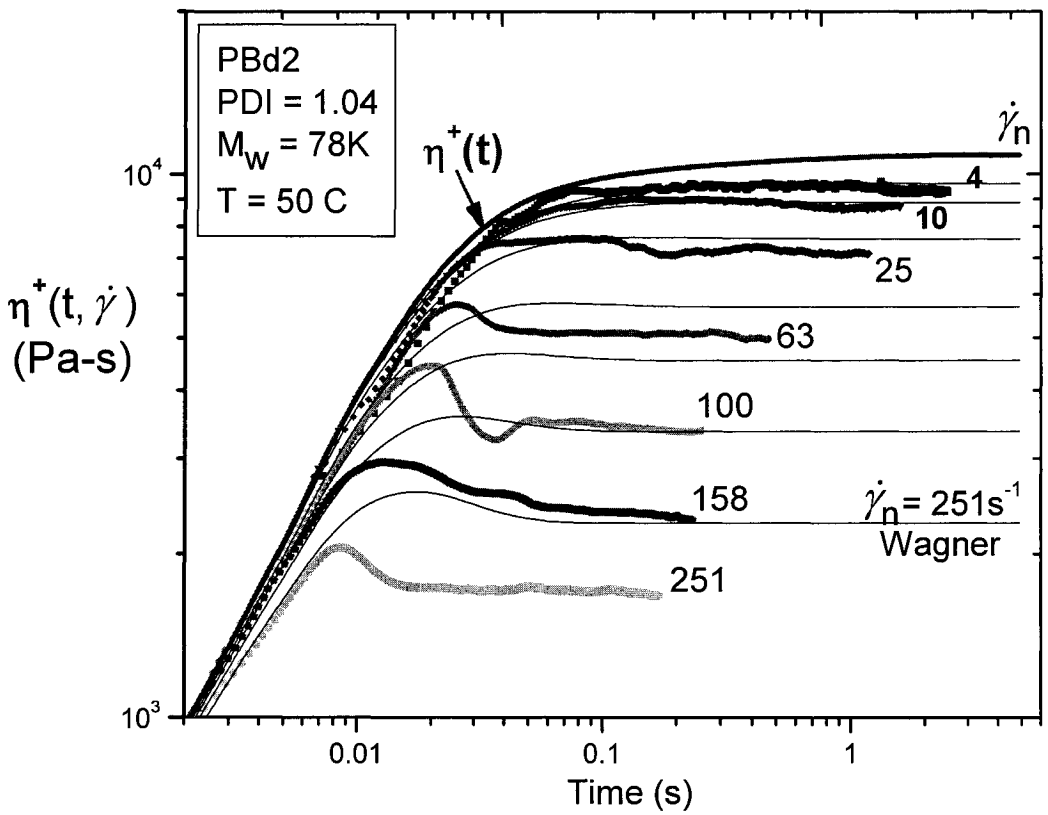

Figure 3-6 Shear stress growth function at several shear rates for PBd2 and comparison with predictions of Wagner's model.

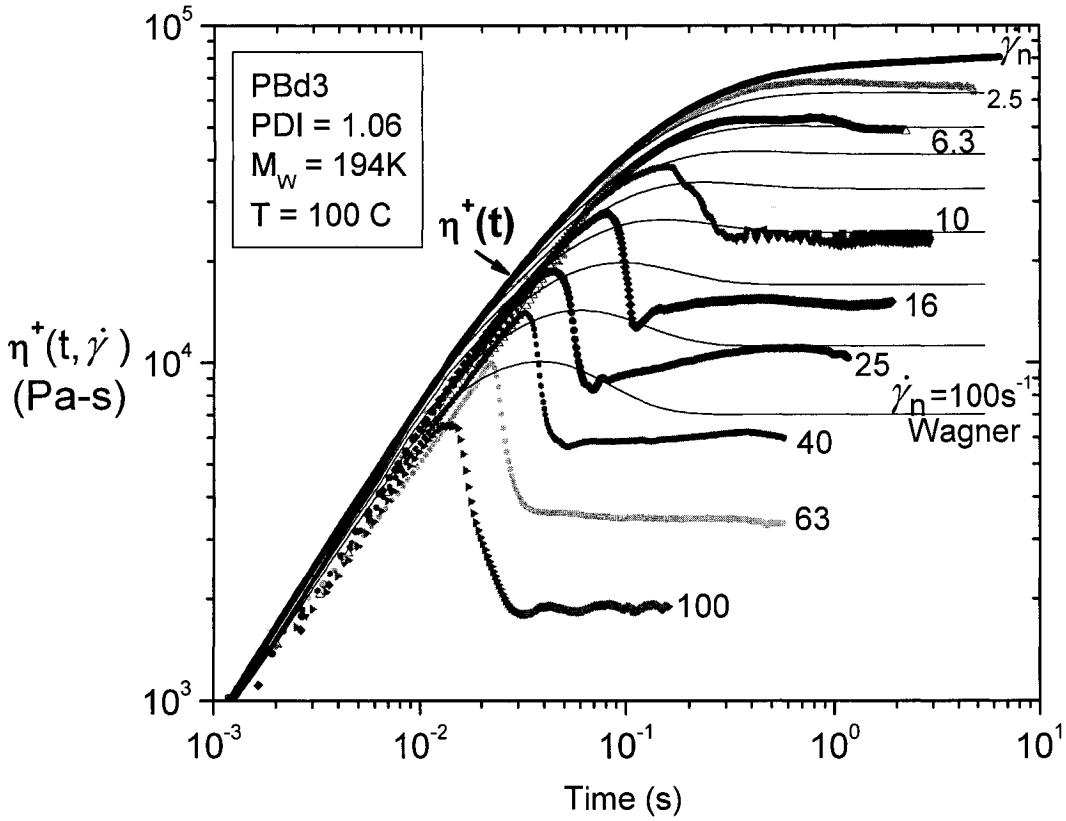

Figure 3-7 Shear stress growth function at several shear rates for PBd3 and comparisons with predictions of Wagner's model.

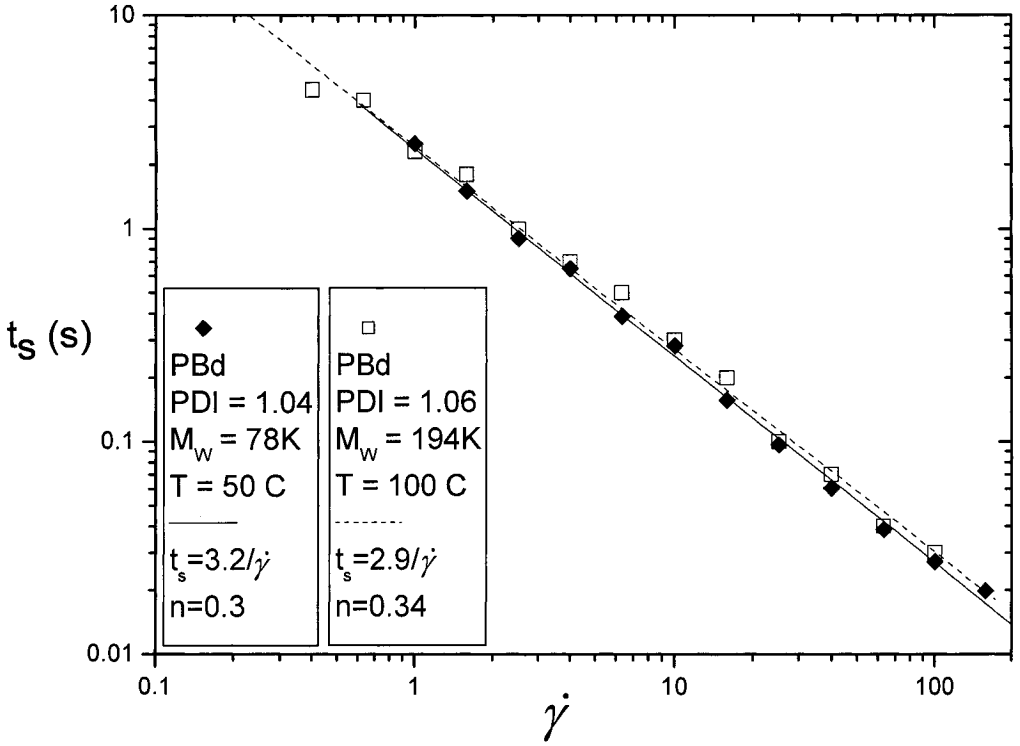

Figure 3-8 Time to reach the maximum shear stress as a function of shear rate.

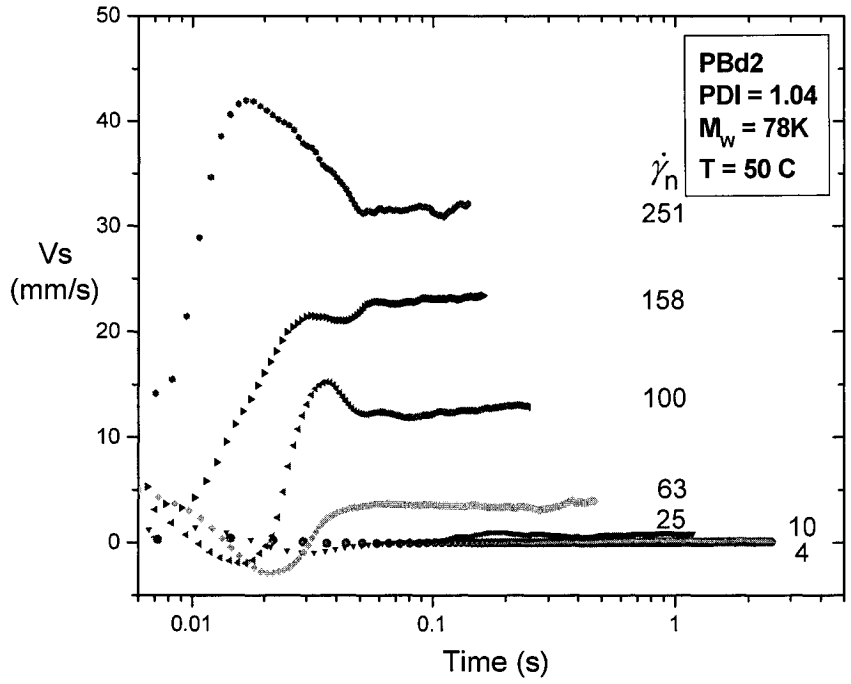

Figure 3-9 Slip velocity as a function of time at several nominal shear rates for PBd2.

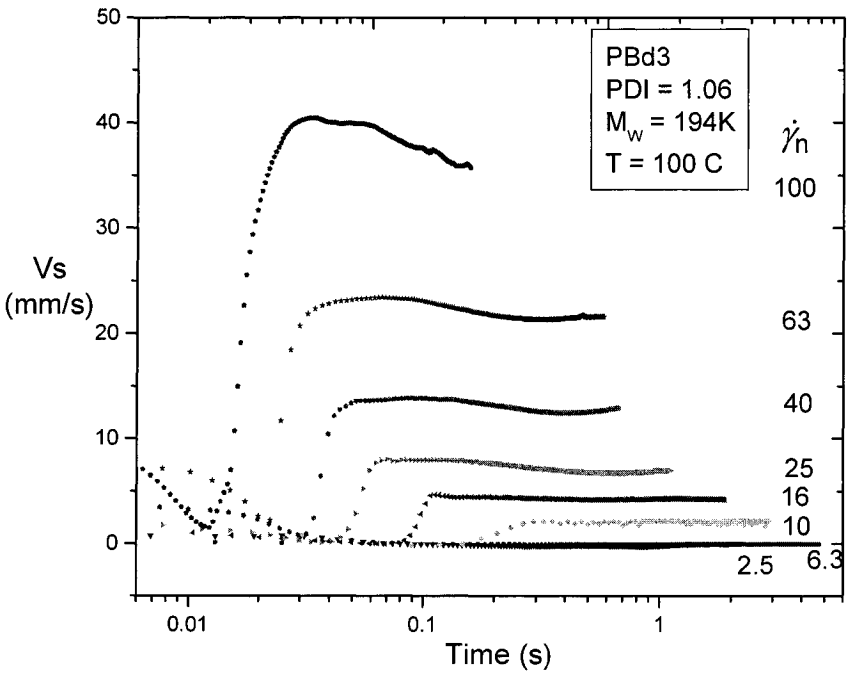

Figure 3-10 Slip velocity as a function of time at several nominal shear rates for PBd3.

3.3.2 Steady-State Viscosity and Wall Slip

A comparison of viscosity values estimated using the Cox-Merz rule with those calculated using Wagner's model is shown in Fig. 3-11. With deviations of less than 10%, the agreement over two decades of shear rate is deemed adequate to validate the use of Eq. 1-41.

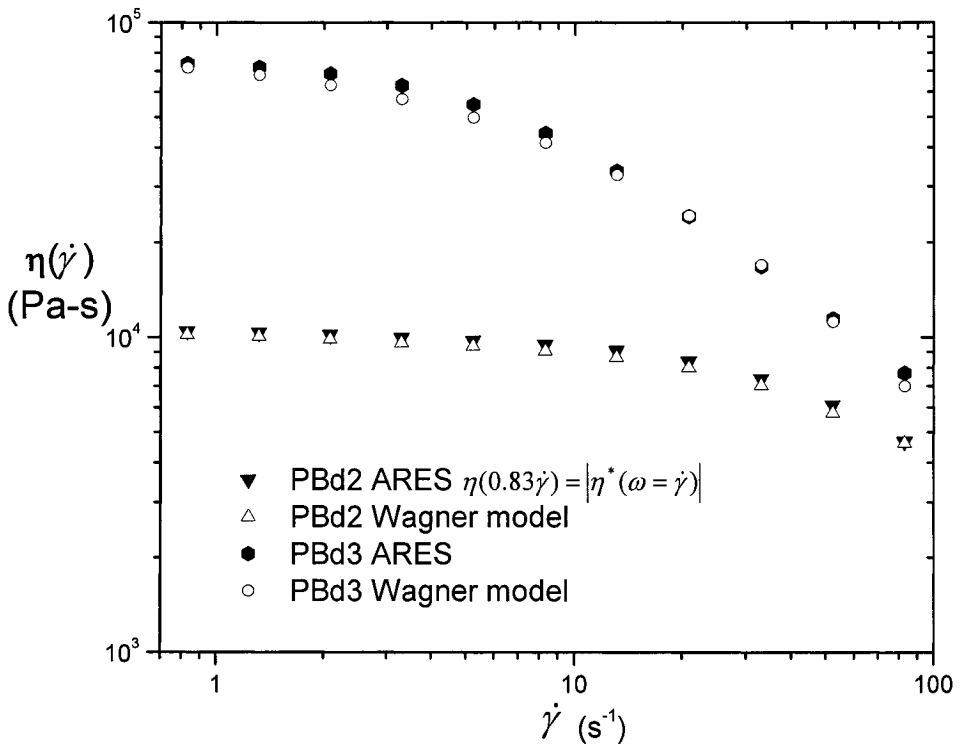

Figure 3-11 Comparison of viscosity values inferred from the complex viscosity with predictions of the Wagner model

According to Section 2.3, the flow curves for no-slip behavior obtained from ARES and slip behavior with steel/steel and glass/steel plates obtained from SPR are shown in Figures 3-13 and 3-14. The slip velocities for glass and steel substrates were then calculated using Eqs. 2-10 and 2-11 and are shown as functions of shear stress in Figures 3-15 and 3-16. The steady-state slip velocities obtained from Figures 3-9 and 3-10 using Wagner's model are also shown in Figures 3-15 and 3-16, and the agreement is deemed satisfactory.

To facilitate the use of the procedure of Section 2.3 to establish the SPR stress response for glass/glass plates in terms of $\dot{\gamma}$, power laws were fitted to the no-slip flow curves, as shown in Fig. 3-12. It was not possible to describe an entire curve using a single set of power-law parameters, and as shown in Fig. 3-12 several power-law segments were used to fit each curve. The steady-state shear stress for glass/glass plates was thus calculated, and the resulting flow curves for glass/glass plates as functions of nominal shear rate are shown in Figs. 3-13 and 3-14.

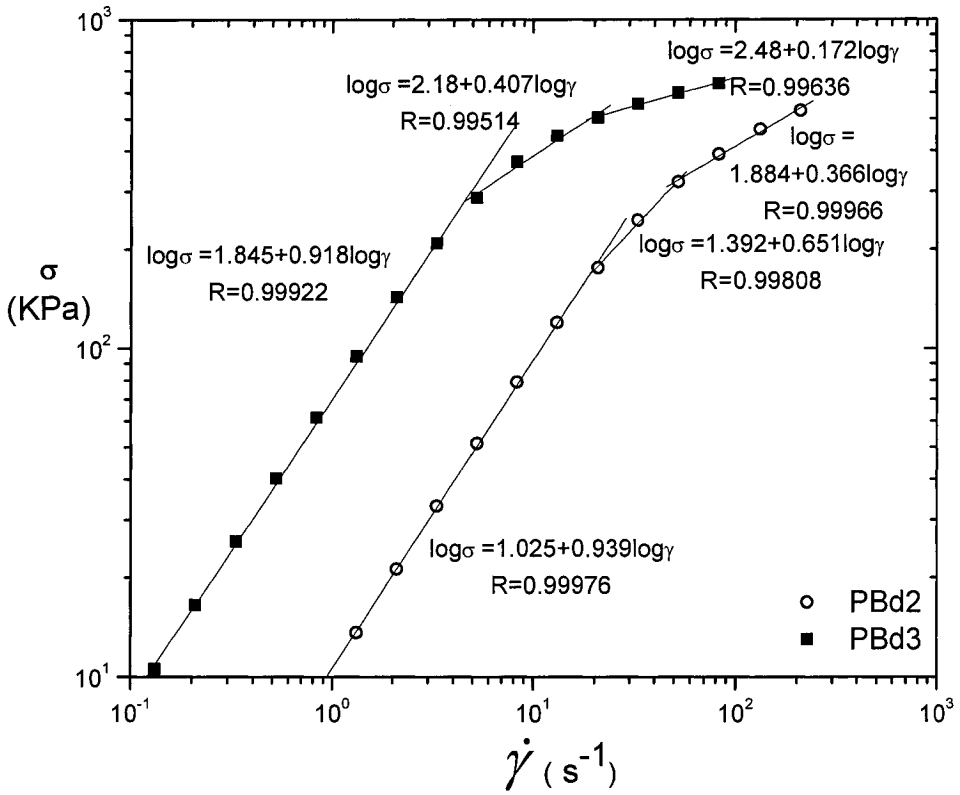

Figure 3-12 Piece-wise power-law fitting of no-slip flow curves.

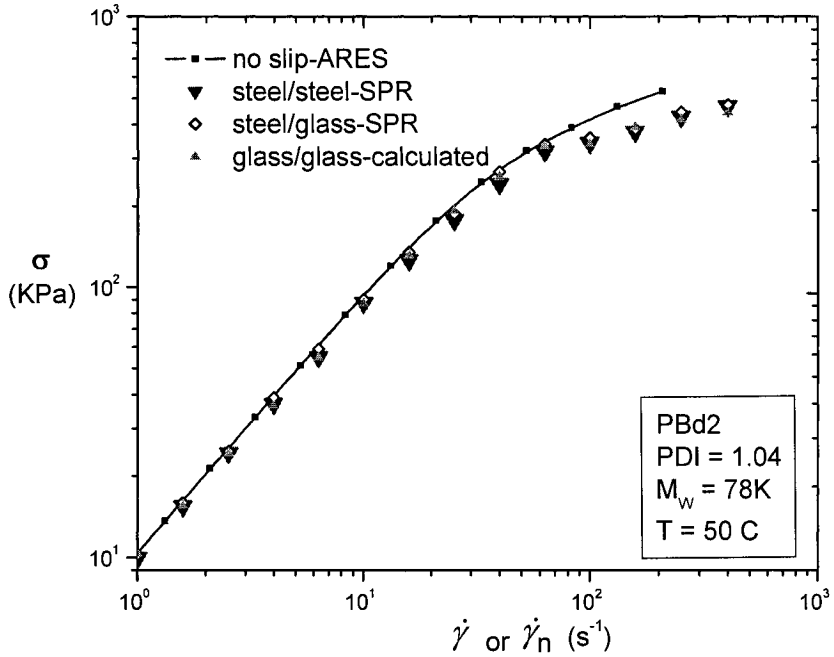

Figure 3-13 Flow curves for no-slip condition slip conditions for PBd2.

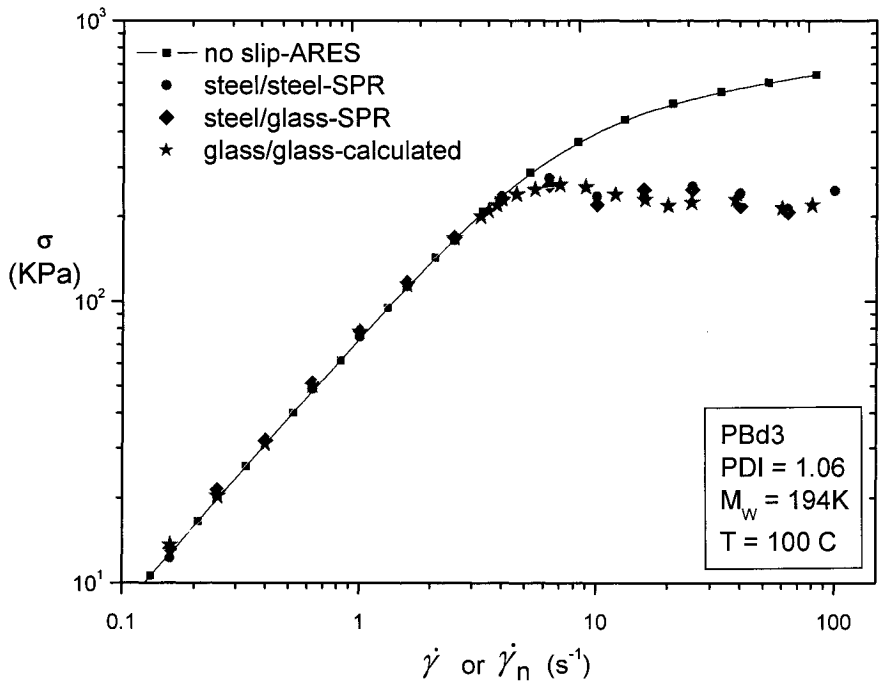

Figure 3-14 Flow curves for no-slip and slip conditions for PBd3.

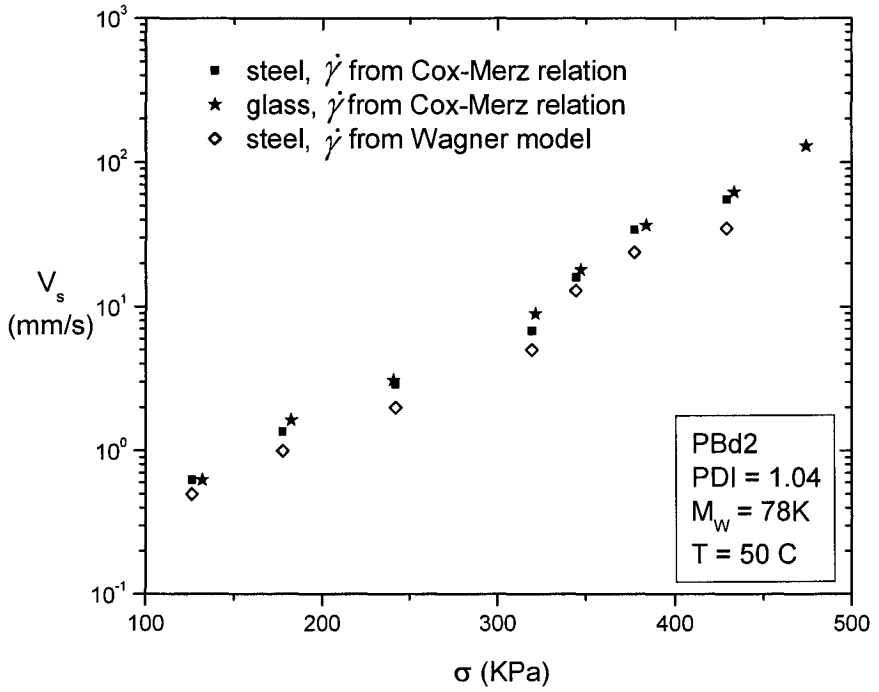

Figure 3-15 Slip velocity vs. shear stress for PBd2.

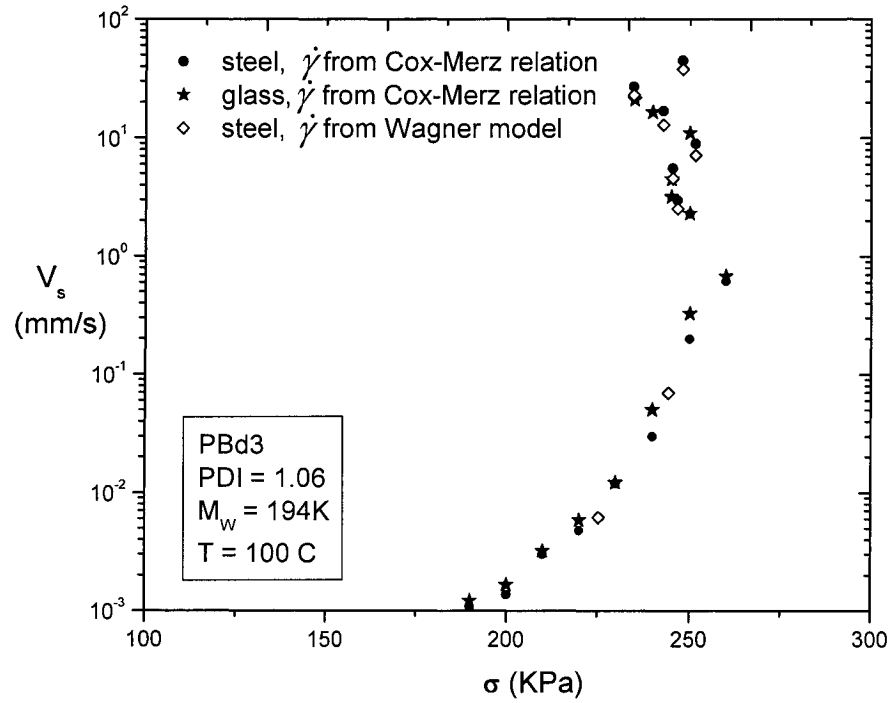

Figure 3-16 Slip velocity vs. shear stress for PBd3.

Figures 3-13 and 3-14 show that the SPR steady-state stresses for both PBds diverge from the no-slip flow curves at a certain stress of about 230 kPa and a nominal shear rate of about 5 s^{-1}. This can be explained in terms of a shear-induced disentanglement between molecules strongly adsorbed at the wall and those in the bulk, which was described in Section 1.4.

The slip behaviors of the two PBds above the critical stress were distinct from each other. For PBd2, the steady-state stress continued to increase with shear rate but with a smaller slope. This indicates a moderate increase of slip velocity over the higher range of shear stress studied, following the approximate power law $V_s \sim \sigma^{4.0}$, as shown by Figure 3-15. Unlike PBd2, at stresses above the critical value, PBd3 exhibited a dramatic increase of slip velocity. In this regime, the shear stress seems to become saturated at its critical value instead of continuously increasing as in the case of PBd2. The behavior shown in Figure 3-16 indicates the presence of very strong slip. Referring to Table 2-1, one concludes that slip behaviour is dependent on the molecular-weight and entanglement density. The drastic slip that occurs above the critical stress for PBd3 can be associated with the fact that the molecular weight and entanglement density of PBd3 are nearly three times those of PBd2.

When comparing the flow curves obtained with steel/steel and steel/glass assemblies, there is very little difference between the two substrate materials. Although glass has a somewhat lower surface energy than steel, the results imply that the interfacial interactions between polymer and steel are remarkably similar to those between polymer and glass over the studied range of shear stress. Therefore, the stresses and slip velocities for steel and glass surfaces are nearly identical, as shown in Figures 3-15 and 3-16. Discrepancies between slip velocities calculated from Wagner model and those inferred directly from stress measurements are thought to arise from errors in the viscosity values predicted by Wagner's equation.

Viscosity values based on SPR data corrected for slip are compared with those inferred from the complex viscosity in Figures 3-17 and 3-18. The zero-shear viscosity η_0 and the zero-shear first normal stress coefficient $\Psi_{1,0}$ calculated using Eqs. 1-13 and 1-14 are also shown. Agreement between the two sets of viscosity points suggests that the calculations were carried out in a correct manner.

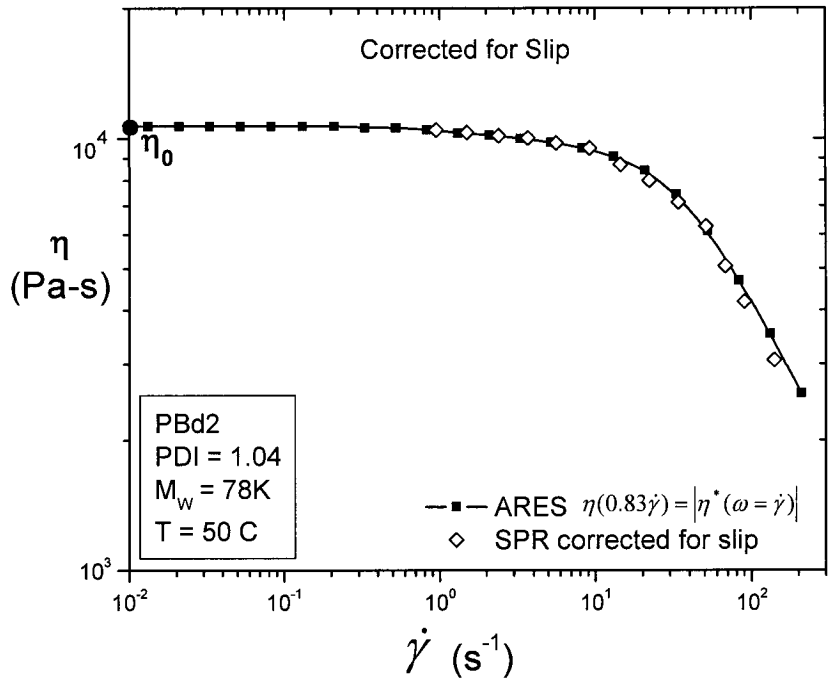

Figure 3-17 Slip-corrected viscosity for PBd2.

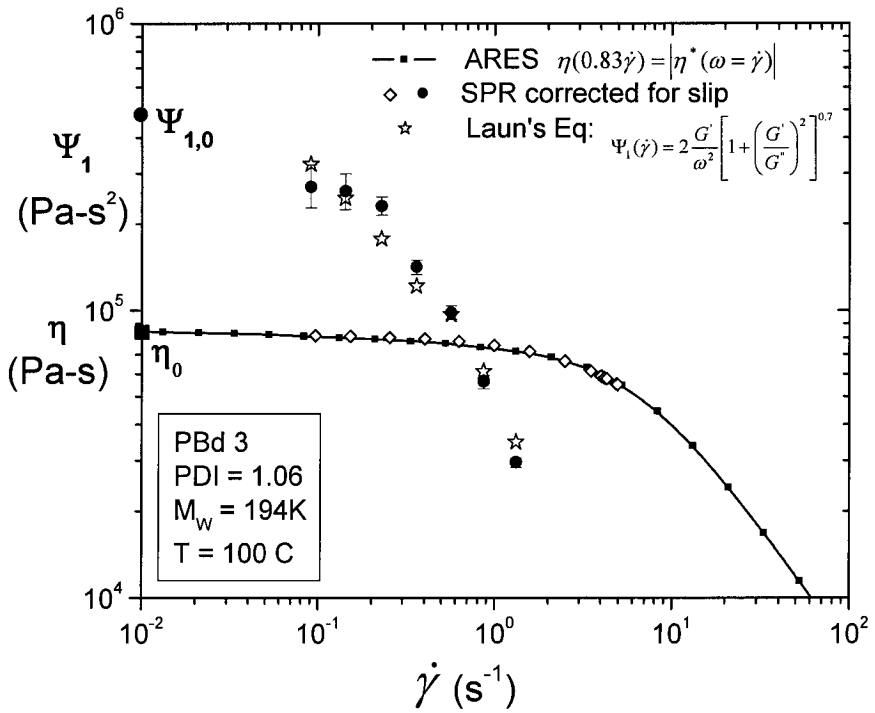

Figure 3-18 Viscosity and first normal stress coefficient for PBd3.

3.3.3 Measurements of the First Normal Stress Difference

The first normal stress was measured using the normal stress transducer shown in Figure 2-5. However, the reproducibility of the start-up transient response is much more chaotic than that of shear stress. The high molecular-weight PBd3 exhibits a well-defined steady-state normal stress at moderate nominal shear rates, as shown in Figure 3-19 but the lower molecular weight PBd2 did not exhibit stable behavior. While Figure 3-18 indicates that the two low-shear-rate Ψ_1 points are not approaching the zero-shear value calculated using Eq. 1-14, we note that those points are subject to substantial uncertainty due to the low stress level. The star points in Figure 3-18 were calculated using Eq. 3-1, which is Laun's relationship between $\Psi_1(\dot{\gamma})$ and the components of the complex modulus [31]. The deviations between the experimental data and the values calculated using Laun's equation are less than 20%.

$$\Psi_1(\dot{\gamma}) = 2\frac{G'}{\omega^2}\left[1+\left(\frac{G'}{G''}\right)^2\right]^{0.7} \tag{3-1}$$

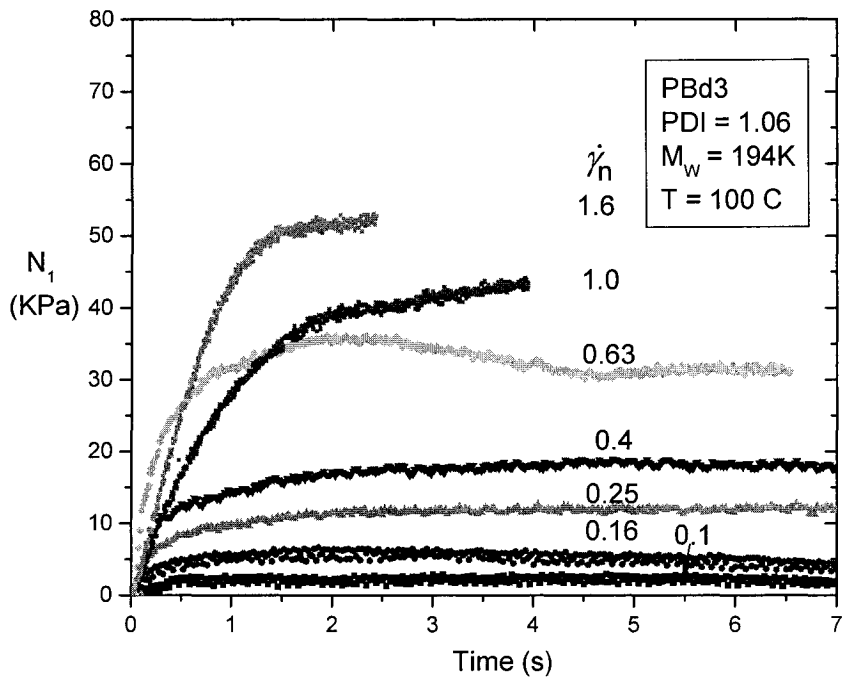

Figure 3-19 Normal stress response for PBd3 at startup of steady simple shear.

To establish the validity of the SPR-NST technique for the measurement of N_1 at high shear rates, a comparison was made of our data with those obtained using a Lodge Stressmeter [34,35]. This is a flow-through slit rheometer in which both the hole pressure and the true wall pressure are measured, and the difference is related to N_1 by equations derived by Higashitani and Pritchard [36]. Lodge [37] kindly provided us with normal stress data at 208°C for Styron 678, a commercial polystyrene manufactured by the Dow Chemical Co. He has published viscosity data for this polymer [35]. For our measurements, samples were vacuum dried at 50°C overnight before use to eliminate absorbed gasses and avoid the formation of bubbles on heating. Figure 3-20 shows time-dependent N_1 values at high shear rates using the NST. We note that the expected stress overshoot is not present at any shear rate. It is believed that this results from the fact that the sample must come to bulk density equilibrium with the normal pressure field before the stresses are rheologically meaningful. This requires that the melt be pressed against the side rails and slightly compressed before the data are useful. However, there are well-defined steady-state values, and these are compared with those measured using the Stressmeter in Figure 3-21. The agreement is deemed satisfactory, and this suggests that both the Stressmeter and the NST developed for measuring N_1 in the SPR provide reliable data for molten plastics at shear rates above the moderate regime. To our knowledge, this is the first time that high-shear-rate normal stress data from instruments of different types have been found to agree. By analogy with Figure 3-18, Figure 3-22 shows the first normal stress coefficient as a function of shear rate for Styron 678. Also shown is the zero-shear rate value calculated from the linear spectrum using Eq. 1-14, which appears to be consistent with the high-shear rate data.

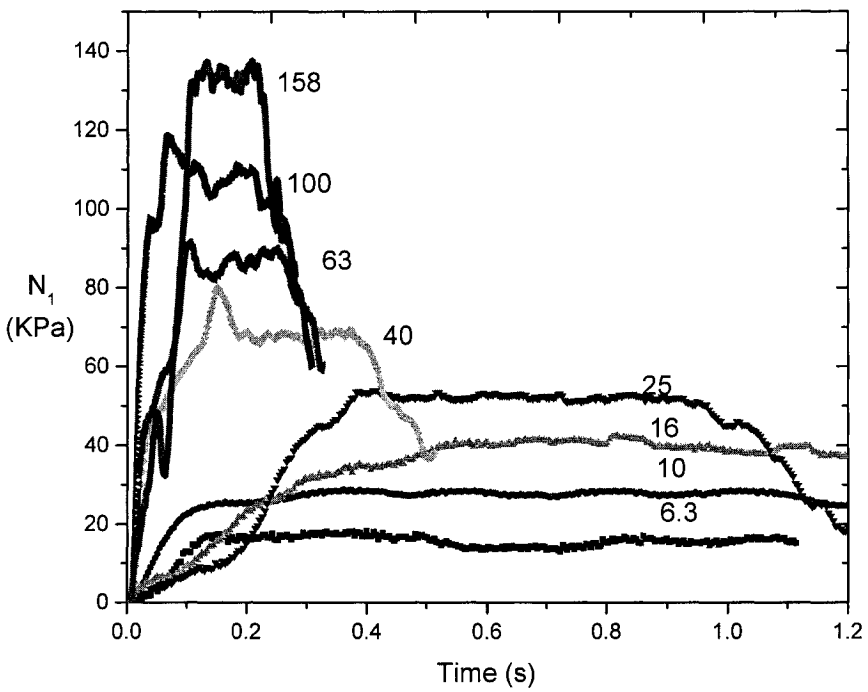

Figure 3-20 Normal stress response for PS 678 in startup of steady simple shear.

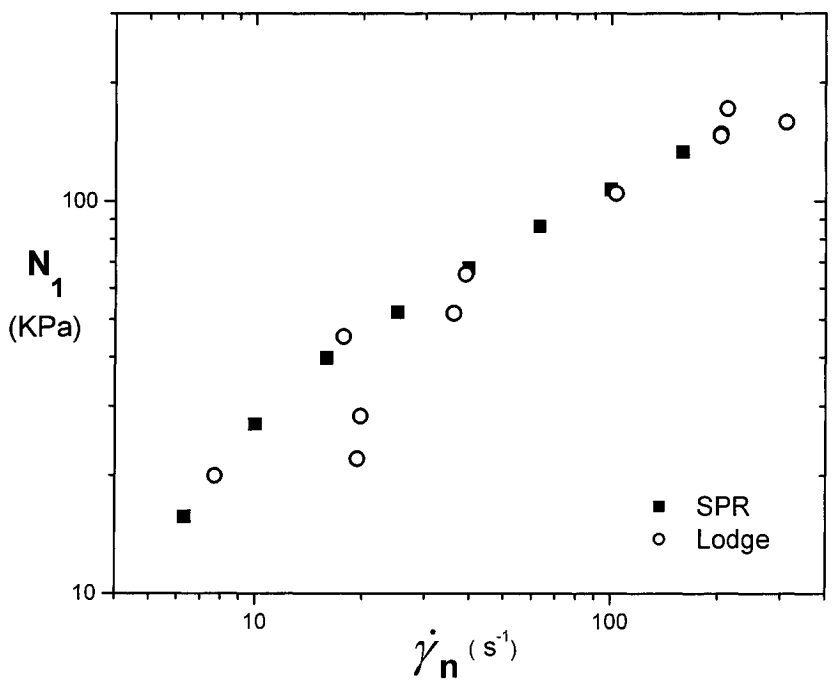

Figure 3-21 Steady state values of N_1 at several shear rates: comparison of SPR data with those obtained using a Lodge Stressmeter [37].

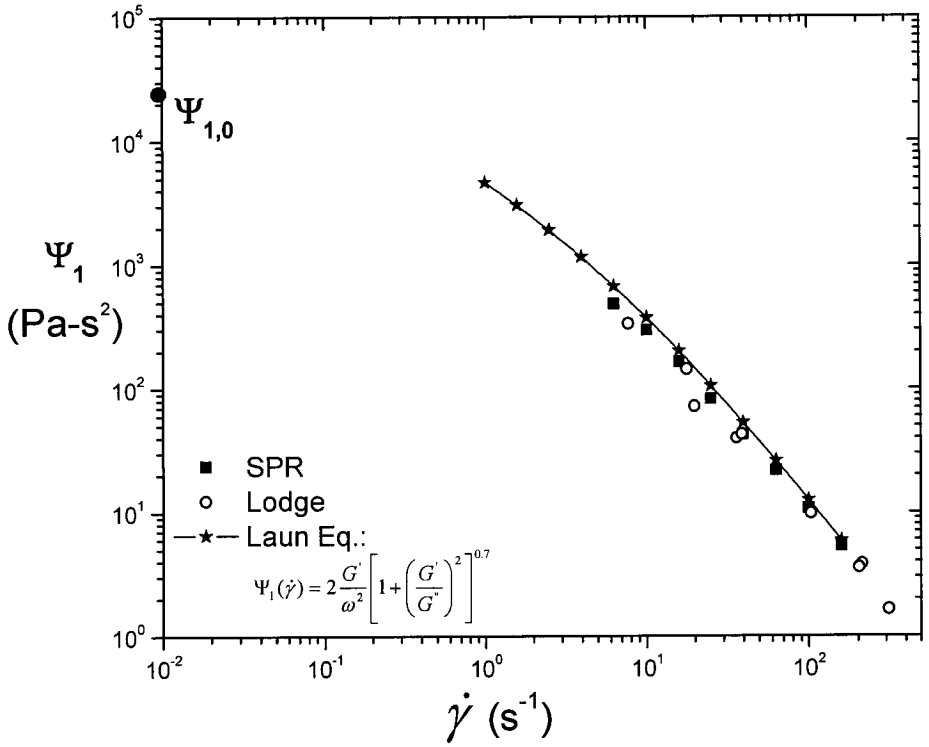

Figure 3-22 The first normal stress coefficient for Styron 678.

3.4 Stress Relaxation

3.4.1 Relaxation Moduli

Eqs.1-26 and1-29 imply that if the logarithm of the nonlinear modulus, determined by measuring $\sigma(t)/\gamma$ and $N_1(t)/\gamma^2$, is plotted as a function of the logarithm of time, the curves for various strains can be brought together by means of vertical shifts. Typical shear stress and first normal stress relaxation moduli $G(t,\gamma)$ and $G_{N1}(t,\gamma)$ at various strain magnitudes are shown in Figures 3-23 to 3-26. The error due to the non-zero rise time was corrected by use of Eq. 2-13.

As seen from the Figs. 3-23 to 3-26 relaxation moduli for strains up to 0.63 superpose without shifting, which implies that at these strains this material exhibits linear viscoelasticity and that the resulting curve is the linear relaxation modulus $G(t)$. As the strain is increased, the relaxation curves deviate from the linear behaviour and fall successively further below it. The long-time ends of the nonlinear modulus curves can be superposed by means of a vertical shift, as shown in Figures 3-27 and 3-28. The value of the time after which superposability is observed is usually called λ_k in the literature. This behavior demonstrates time-strain separability as described by Eqs. 1-26 and 1-29. The tube model explains this as a manifestation of chain stretch relaxation, i.e., time-dependent retraction of a molecule in its tube [2]. At the longest times, the stress signal becomes very small, and the signal-to-noise ratio becomes unfavourable, as shown in Figures 3-25 and 3-26.

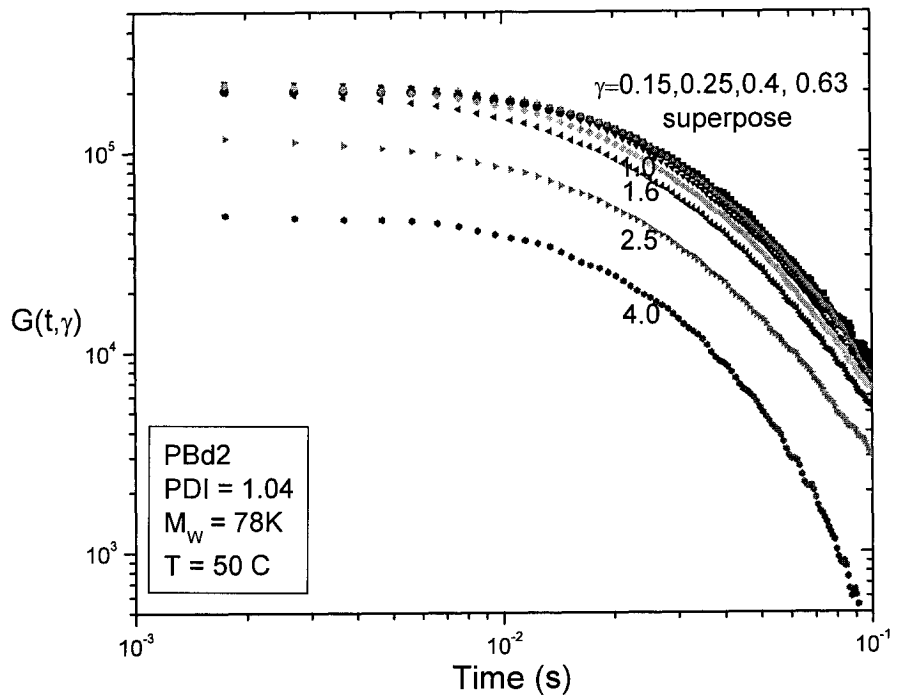

Figure 3-23 Nonlinear shear stress relaxation moduli for PBd2.

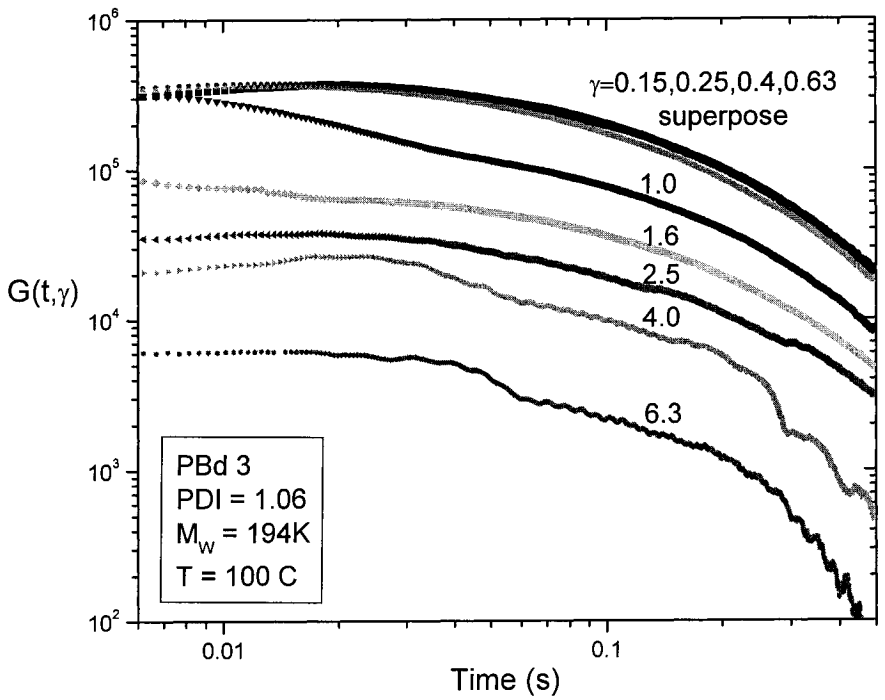

Figure 3-24 Nonlinear shear stress relaxation moduli for PBd3.

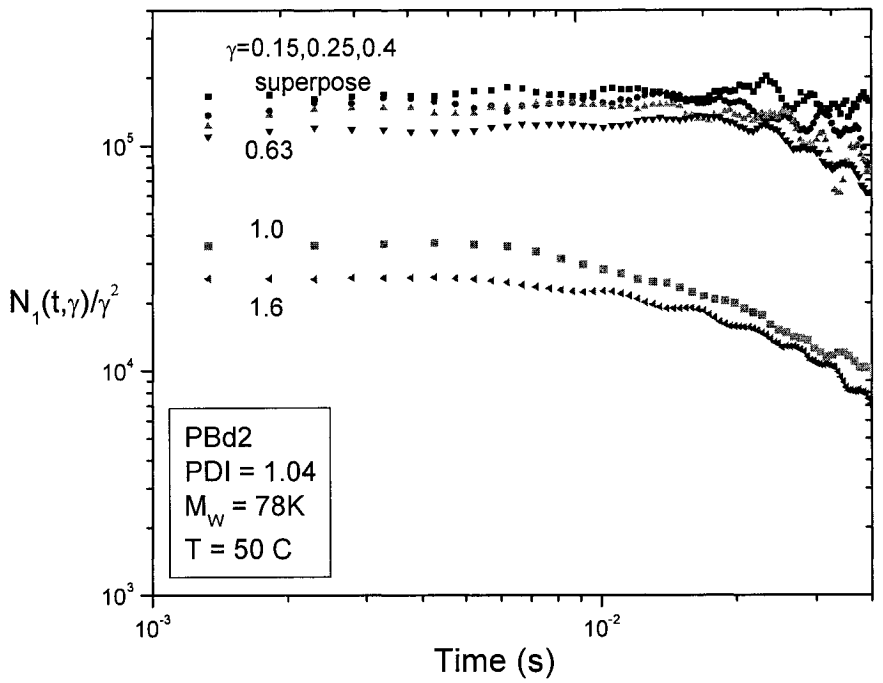

Figure 3-25 Nonlinear first normal stress relaxation moduli for PBd2.

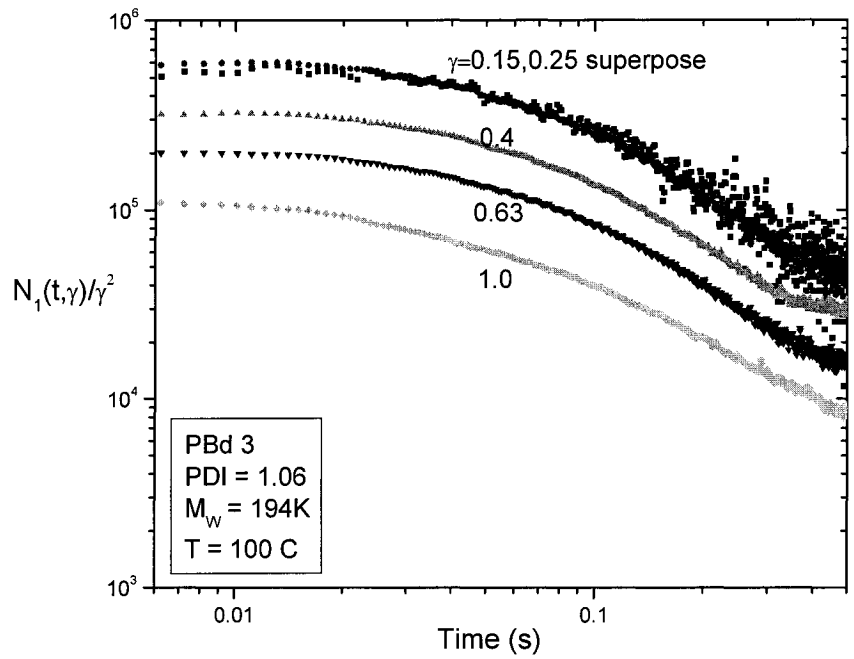

Figure 3-26 First normal stress relaxation modulus for PBd3.

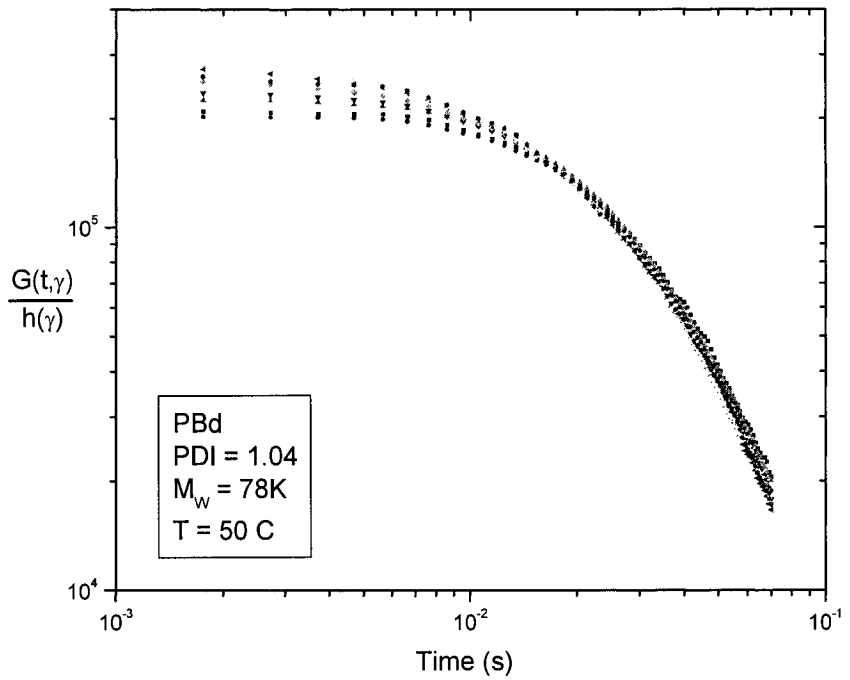

Figure 3-27 Shifted shear stress relaxation moduli for Figure 3-20.

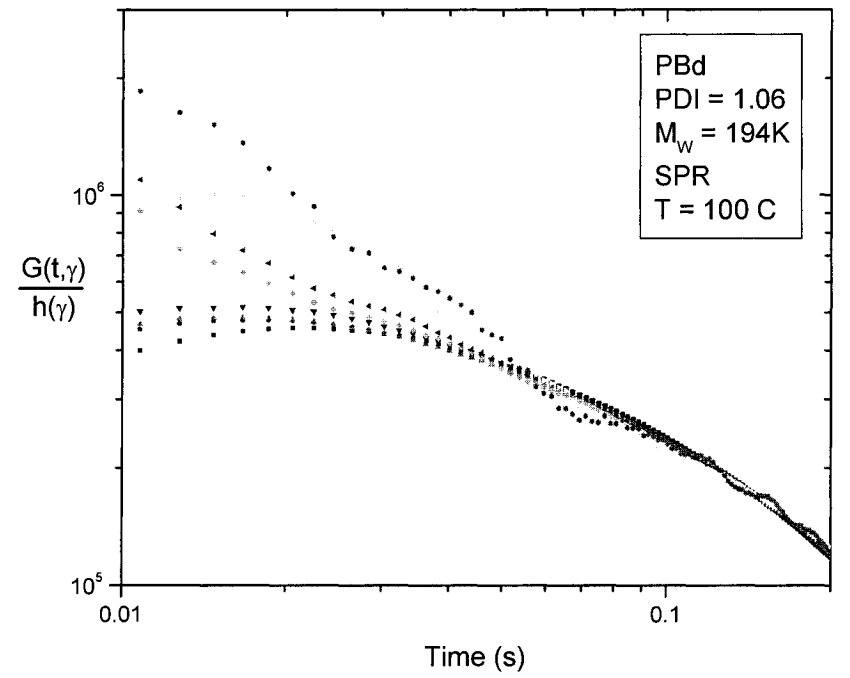

Figure 3-28 Shifted shear stress relaxation moduli for Figure 3-21.

3.4.2 Damping Function Determination and Wall Slip

According to Eqs. 1-26 and 1-29, the value of the damping function at each strain can be determined from the shift factors for the nonlinear relaxation moduli. Because slip was suspected, the strain was calculated using the plate displacement ($\gamma = V/h$) as well as the Lodge-Meissner relation ($\gamma = N_1/\sigma$). Figure 3-29 compares the nominal strain with that based on the Lodge-Meissner relation. For strains smaller than 0.25, the two strains agree perfectly, and up to a strain of one, the stress ratio N_1/σ is never more than 20% below the nominal strain. This implies that slip was not a major problem at these small strains.

Figure 3-30 shows the damping function of PBd2 as a function of nominal shear strain in comparison with the prediction of the Doi-Edwards (DE) theory. The good agreement implies that slip was not a major factor over the range of strains involved. However, for PBd3 the value of the strain calculated using the Lodge-Meissner relation falls significantly below the nominal strain when the latter is one, as shown in Figure 3-29.

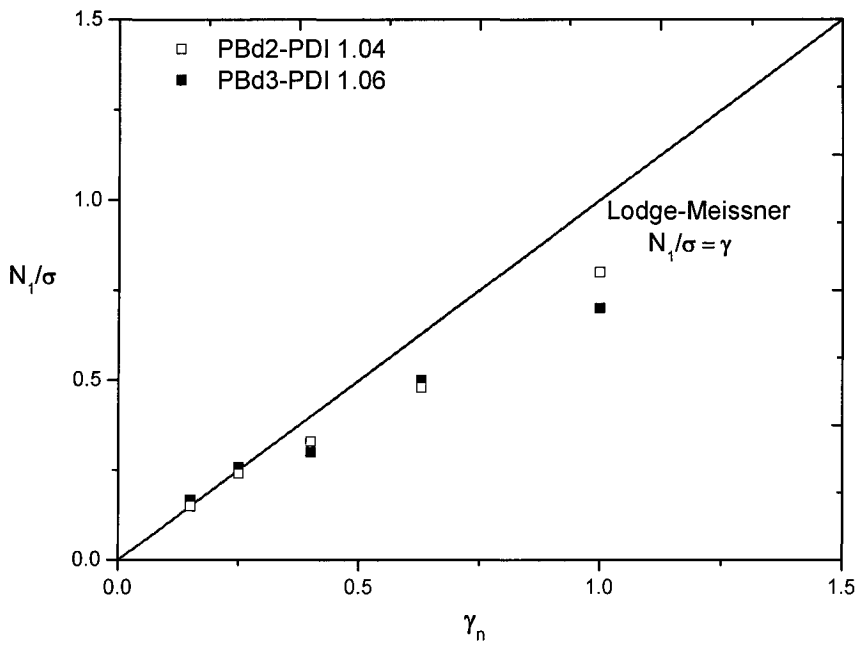

Figure 3-29 N_1/σ versus nominal strain.

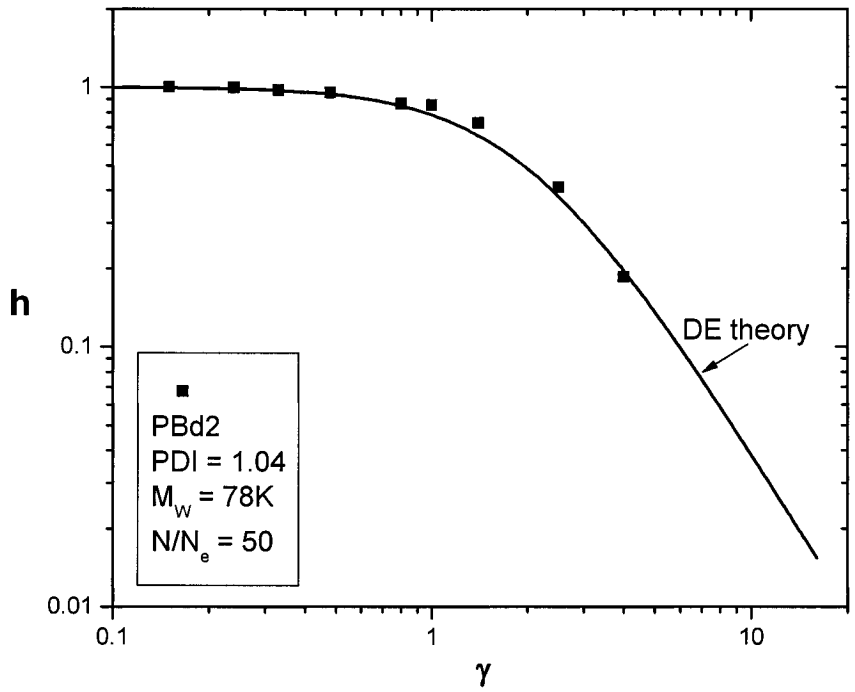

Figure 3-30 Damping function of PBd2 compared with DE theory

Section 3.2.2 indicates that the interfacial interaction between polymer and steel is quite similar to that between polymer and glass. This suggests that the slip displacement of polymer on steel can be revealed visually by the use of a glass stationary plate and used to indicate the true strain for a steel surface when slip occurs. By monitoring marker lines drawn on both sides of a sample of PBd3, the true shear strain resulting from a step displacement of the moving plate could be observed, as shown in Fig. 3-31.

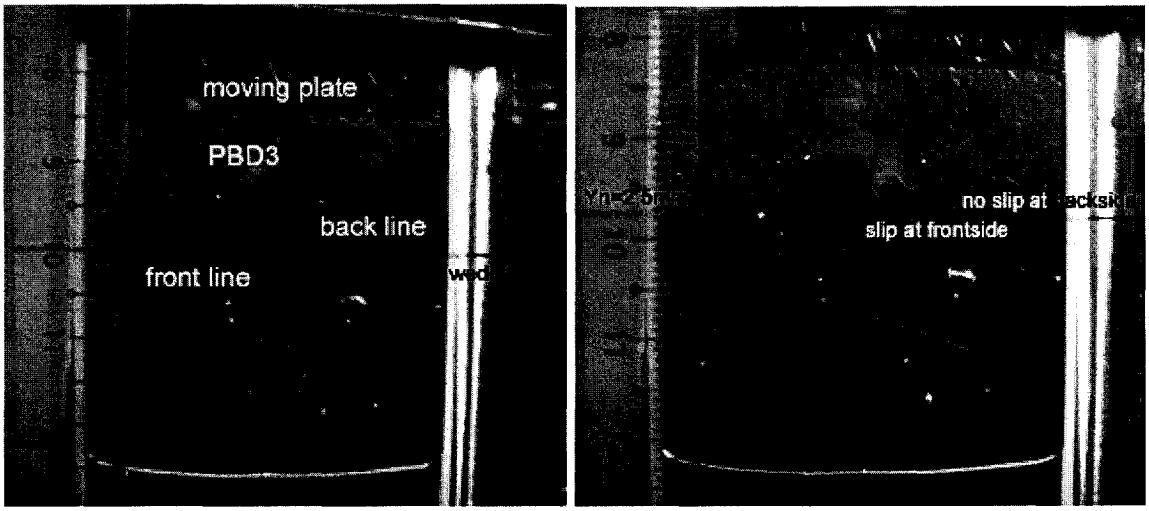

(a) (b)

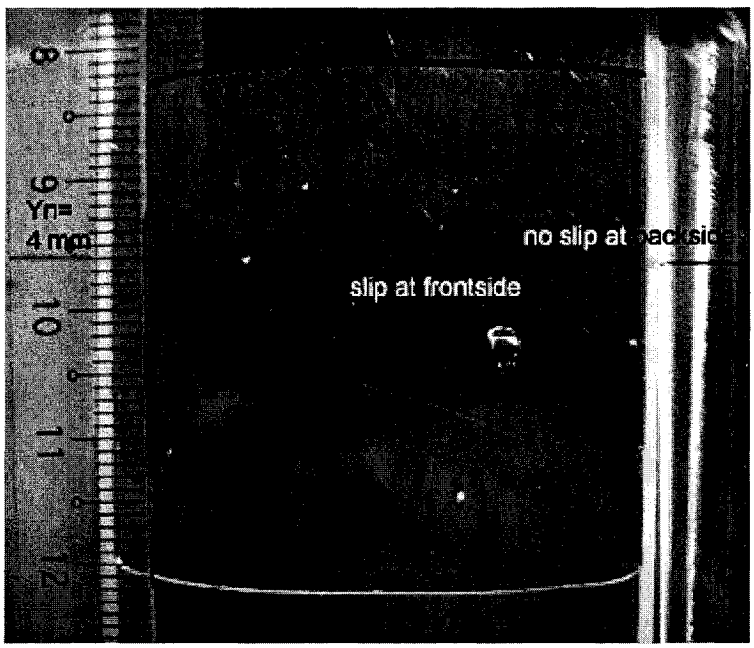

(c)

Figure 3-31 Wall slip of PBb3 as seen through a glass fixed plate with a gap of 1mm: before shear (a) and with moving plate displacements of (b) 2.5 mm and (c) 4.0 mm.

Figure 3-31(a) shows a pre-sheared sample PBd3 in the 1 mm gap between a steel moving plate and a glass fixed plate laterally restrained by two Teflon rails. The colored straight lines on each side of sample are first lined up with the scale on the glass plate and the thin black line on the wedges of moving plate. After plate displacements of 2.5 mm and 4 mm, the appearances of the sample are as shown in (b) and (c). The marker line on the back of sample aligns exactly with the line on the wedge of the moving plate,

indicating that no slip occurred at the polymer/steel interface. However, the separation of the front (red) marker lines indicates that some slip has occurred. The actual strain imposed on the sample can be determined from the distance between the targeted strain indicator (the line on the wedge) and the slip-shifted line on the front side. For purposed of calculating the damping function for PBd3, the strain for $\gamma<1$ was assumed to be equal to the stress ratio N_1/σ, and at higher strains the strain was based on observations using the glass plate. The resulting damping function is shown in Fig. 3-32.

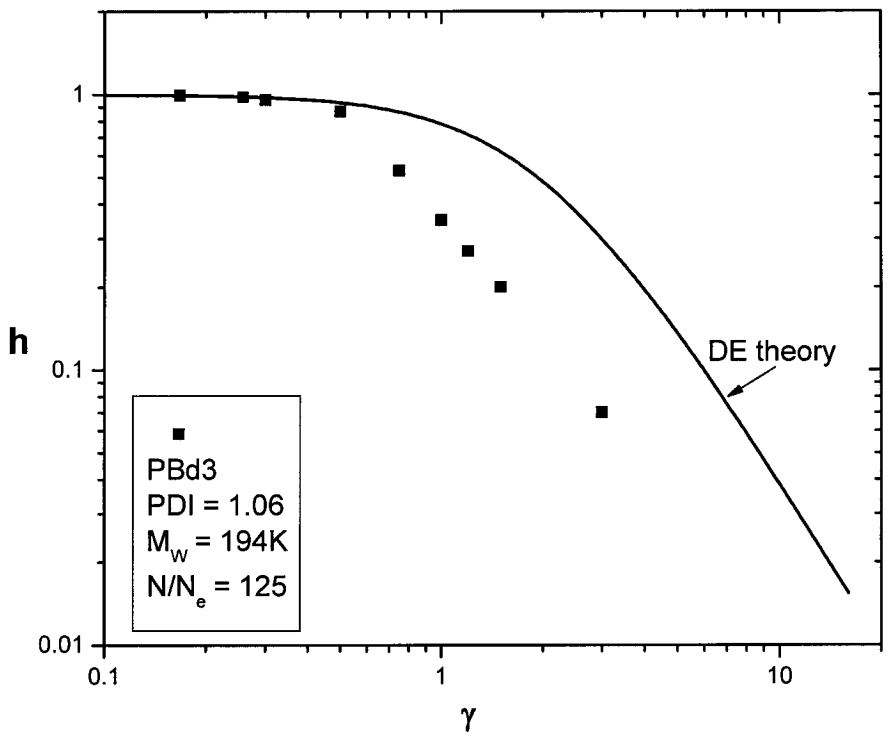

Figure 3-32 Damping function of PBd3: strain equal to stress ratio for low-strain portion and calculated using the slip correction for the moderate-strain portion.

Figure 3-30 shows that the shear damping function of PBd2 is in accord with DE prediction, which is the expected result for a well entangled polymer [38,39]. However, the shear damping function of the more entangled sample, PBd3 (N/N_e=125), indicates more strain-softening than predicted by the theory at strains greater than one. A molecular interpretation of this phenomenon has been given by Islam *et al.* [40] in terms of coupling between polymer segment orientation and tube equilibration.

Chapter 4 Conclusions and Contributions to Knowledge

4.1 Conclusions

1. Start-up of steady simple shear experiments on PBd2 and PBd3 exhibit typical nonlinear shear stress growth curves.

2. Comparisons of experimental data with predictions of the Wagner model show that the model provides good predictions for most of the quantitative aspects of start-up behaviour, including the stress overshoot, and reveal the presence of wall slip in fast shear flows. Time-dependent slip velocities were inferred from the difference between the experimental data and the model predictions. Time-dependent slip data for molten polymers have never before been reported.

3. Start-up of steady simple shear experiments also reveals that the critical shear stress for the onset of slip is about 230kPa for both the polymers studied. This confirms a previous suggestion that the critical stress is independent of molecular weight and entanglement density but proportional to the plateau modulus.

4. The slip behaviors of the two PBds are different from each other. This implies that slip behaviour depends on molecular weight; we note that M_w and N/N_e of PBd3 are nearly three times larger than those of PBd2. This supports the hypothesis that slip involves a shear-induced disentanglement between molecules strongly adsorbed at the wall and those in the bulk in highly entangled polymers

5. The apparent flow curves for steel surface and glass surface are very similar over the entire range of stresses studied for both PBds. This implies that slip occurs in a similar manner on both steel and glass surfaces. This means that the slip displacements observed using a transparent glass plate can be used to correct data obtained using a steel plate.

6. PBd3 exhibits a well-defined steady-state normal stress response at moderate shear rates. Modification of the rheometer will be necessary to make possible measurements on materials of this type. The good agreement of steady-state N_1 measured by SPR with that from Lodge Stressmeter Rheometer verifies that the technique developed for measuring N_1 using SPR is able to work for the plastics at shear rates above the moderate regime.

7. Step strain data were used to construct curves of damping function. Time-strain separability failed at short times for both PBds, and tube theory explains this as a manifestation of the time-dependent retraction resulting from chain stretch.

8. Agreement of the damping function of PBd2 with the prediction of the Doi-Edwards theory, as well as the validity of the Lodge-Meissner relation in the lower strain region, indicate the absence of slip for PBd2 for all the step strain shear experiments. This seems to agree with Vinogradov's observation that slip in PBd does not occur at this value of M_w/M_e [15].

9. Wall slip of PBd3 in large-strain step shear manifests itself through a decrease in the amplitude of shear strain as observed using a marker technique with a glass plate. The damping function of the highly entangled sample PBd3 (N/N_e=125) is more straining-softening than the Doi-Edwards prediction at strains greater than one.

4.2 Contributions to knowledge

It was demonstrated how a sliding plate rheometer equipped with a shear stress transducer can be used to study the nonlinear viscoelastic behavior of highly entangled molten polymers. A technique for using this apparatus to measure the first normal stress difference at high strain rates was developed. This marks the first time that a laboratory instrument has been used to make such measurements.

References

1. de Gennes, P.G., "Reptation of a Polymer Chain in the Presence of Fixed Obstacles." *J. Chem. Phys.*, 55, 572-579 (1971).

2. Doi, M., Edwards, S.F., "The Theory of Polymer Dynamics". Chapter 6: "Dynamics of a Polymer in a Fixed Network", p.191-204, Oxford: Clarendon (1986).

3. Dealy, J.M., Wissbrun, K.F., "Melt rheology and its role in plastics processing", Chapter 3.4: "Finite measure of strain" p. 108-114, Kluwer Academic Publishers

4. Lodge, A.S., "Elastic Liquids: an introductory vector treatment of finite-strain polymer rheology", Chapter 6: "A Rubberlike Liquid", p. 101-120, Academic Press, NY (1964).

5. Wagner, M.H., "Analysis of time-dependent non-linear stress-growth data for shear and elongational flow of a low-density branched polyethylene melt." *Rheol. Acta*, 15(2), 136-142 (1976).

6. Lodge, A.S., Meissner, J., "Use of instantaneous strains, superposed on shear and elongational flows of polymeric liquids, to test the Gaussian network hypothesis and to estimate the segment concentration and its variation during flow." *Rheol. Acta*, 11(3-4), 351-352 (1972).

7. Lodge, A.S., "A classification of constitutive equations based on stress relaxation predictions for the single-jump shear strain experiment." *J. Non-Newt. Fl. Mech.*, 14, 67-83 (1984).

8. Graessley, W.W., Park, W.S., Crawley, R.L., "Experimental tests of constitutive relations for polymers undergoing uniaxial shear flows." *Rheol. Acta.*, 16(3), 291-301 (1977).

9. Koran F., Dealy, J.M., "Wall slip of polyisobutylene: Interfacial and pressure effects." *J. Rheol.*, 43, 1291-1306 (1999).

10. Dealy J. M., "Rupture of Molten Polymers, Summary of the Present State of Knowledge", Department of Chemical Engineering, McGill University (2000).

11. Wang, S.Q., "Molecular transitions and dynamics at polymer/wall interfaces: origins of flow instabilities and wall slip." *Advances in Polym. Sci.*, 138, 227-275 (1999).

12. Kissi, N. El, Piau, J.M., section III.4, p. 357 of "Rheology for Polymer Melt Processing", edited by Piau, J.M., Agassant, J.F., Elsevier, Amsterdam (1996).
13. Wang, S.Q., Drda, P.A., "Superfluid-Like Transition in Capillary Flow of Highly Entangled Linear Polyethylene Melts." *Macromolecules*, 29(7), 2627-2632; "Stick-Slip Transition in Capillary Flow of Polyethylene. 2. Molecular Weight Dependence and Low-Temperature Anomaly.", 29(11), 4115-4119 (1996).
14. Wang, S.Q., Drda, P.A., Inn, Y.W., "Exploring molecular origins of sharkskin, partial slip, and slope change in flow curves of linear low density polyethylene." *J. Rhoel.*, 40, 875-898 (1996).
15. Vinogradov, G.V., "Ultimate regimes of deformation of linear flexible chain fluid polymers", *Polymer*, 18, 1275-1285 (1977).
16. Pearson, D.S., Rochefort, W.E., "Behavior of concentrated polystyrene solutions in large-amplitude oscillating shear fields." *J. Polym. Sci., Polym.Phys.* Ed., 20(1), 83-98 (1982).
17. Larson, R.G., "Instabilities in viscoelastic flows." *Rheol. Acta.*, 31(3), 213-263; "Flow-induced mixing, demixing, and phase transitions in polymeric fluids.", 31(6) 497-520 (1992).
18. Galvin, P.T., Whorlow, R.W., "Time effects in the flow of polymer melts using a biconical viscometer." *J. Appl. Polym. Sci.,* 19(2), 567-583 (1975).
19. Giacomin, A.J., *Ph.D. Thesis*, "A sliding plate melt rheometer incorporating a shear stress transducer." McGill University, Montreal (1987).
20. Giacomin, A.J., Samurkas, T., Dealy, J.M., "A novel sliding plate rheometer for molten plastics." *Polym. Eng. Sci.*, 29(8), 499-504 (1989).
21. Dealy, J.M., Giacomin, A.J., "Sliding plate rheometer", in *Rheological Measurement*, 2nd ed. Chapman and Hall, London, 1998, Chapter 8.
22. Dealy, J.M., "Method of measuring shear stress." US Patent 4,464,928 (1984).
23. Reimers, M.J., Dealy, J.M., "liding plate rheometer studies of concentrated polystyrene solutions: large amplitude oscillatory shear of a very high molecular weight polymer in diethyl phthalate." *J. Rheol.*, 40(1), 167-186 (1996).

24. Reimers, M.J., Dealy, J.M., "Sliding plate rheometer studies of concentrated polystyrene solutions: Nonlinear viscoelasticity and wall slip of two high molecular weight polymers in tricresyl phosphate." *J. Rheol.*, 42(3), 527-548 (1998).
25. Meissner, J., "Experimental methods in polymer melt rheology." *Makromolekulare Chemie, Macromolecular Symposia* 68, 133-146 (1993).
26. Kraft, M., Meissner, J., "Progress and Trends in Rheology." IV, Proceedings of the 4th European Rheological Conference, Dietrich Steinkopff, Darmstadt, 489 (1994).
27. Dealy, J.M., "Method and apparatus for measuring rheological properties of fluid" U.S. Patent No. 4,571,989 (1986).
28. Oakley, J.G., Giacomin, A.J., "A sliding plate normal thrust rheometer for molten plastics." *Polym. Eng. and Sci.*, 34(7), 580-584 (1994).
29. Mhetar, V.R., "Secondary flow of entangled polymer fluids in plane Couette shear." *J.Rheol.*, 40(4), 549-571 (1996).
30. Cox, W.P., Merz, E.H., "Correlation of dynamic and steady-flow viscosities." *J. Polym.Sci.*, 28, 619-622 (1958).
31. Schümmer, P., Worthoff, R.H., "An elementary method for the evaluation of a flow curve." *Chem. Eng. Sci.*, 33(6), 759-763 (1978).
32. Dealy, J.M., Wissbrun, K.F., "Melt rheology and its role in plastics processing", Chapter 5.2.1: "Finite rise time" p. 182, Kluwer Academic Publishers.
33. Zapas, L.J., "Simple shearing flows in polyisobutylene solutions." *J.Res. N. B. S.*, 75(1), 33-40 (1971).
34. Lodge, A.S., "On-line measrurement of elasticity and viscosity in flowing polymeric liquids." *Rheol Acta*, 35, 110-116 (1996)
35. Lodge, A.S. "Normal stress differences from hole pressure measurements", Chapter 10 of *Rheological Measurement*, 2nd edit. Ed. by AA. Collyer and D.W. Clegg, Chapman & Hall, London (1998)
36. Higashitani, K., Pritchard, W.G., "A kinetic calculation of intrinsic errors in pressure measurements using holes" *Trans. Soc. Rheol.* 16, 687-696 (1972)
37. Lodge, A.S., personal communication (2003)

38. Osaki, K., Nishizawa, K., Kurata, M., "Material time constant characterizing the nonlinear viscoelasticity of entangled polymeric systems." *Macromolecules*, 15(4), 1068-1071 (1982).
39. Mead, D.W., Larson, R.G., Doi, M., "A Molecular Theory for Fast Flows of Entangled Polymers." *Macromolecules*, 31(22), 7895-7914 (1998).
40. Islam, M.T., Sanchez-Reyes, J., Archer, L.A., "Nonlinear rheology of highly entangled polymer liquids: Step shear damping function." *J. Rheol.*, 45(1), 61-82 (2001).